

Impact of Enhanced Atmospheric Motion Vectors on HWRP Hurricane Analyses and Forecasts with Different Data Assimilation Configurations

SHIXUAN ZHANG AND ZHAOXIA PU

Department of Atmospheric Sciences, University of Utah, Salt Lake City, Utah

CHRISTOPHER VELDEN

Cooperative Institute for Meteorological Satellite Studies, University of Wisconsin–Madison, Madison, Wisconsin

(Manuscript received 15 May 2017, in final form 25 March 2018)

ABSTRACT

The impacts of enhanced satellite-derived atmospheric motion vectors (AMVs) on the numerical prediction of intensity changes during Hurricanes Gonzalo (2014) and Joaquin (2015) are examined. Enhanced AMVs benefit from special data-processing strategies and are examined for impact on model forecasts via assimilation experiments by employing the National Centers for Environmental Prediction (NCEP) operational Hurricane Weather Research and Forecasting (HWRP) Model using a Gridpoint Statistical Interpolation analysis system (GSI)-based ensemble–variational hybrid system. Two different data assimilation (DA) configurations, one with and one without the use of vortex initialization (VI), are compared. It is found that the assimilation of enhanced AMVs can improve the HWRP track and intensity forecasts of Gonzalo and Joaquin during their intensity change phases. The degree of data impact depends on the DA configuration used. Overall, assimilation of enhanced AMVs in the innermost domain (e.g., storm inner-core region and its immediate vicinity) outperforms other DA configurations, both with and without VI, as it results in better track and intensity forecasts. Compared to the experiment with VI, assimilation of enhanced AMVs without VI reveals more notable data impact on the forecasts of Hurricane Gonzalo, as the VI before DA alters the first guess and reduces the actual number of AMV observations assimilated into the DA system. Even with VI, assimilation of enhanced AMVs in the inner-core region can at least partially mitigate the negative effect of VI on the intensity forecast of Hurricane Gonzalo and alleviate the unrealistic vortex weakening in the simulation by removing unrealistic outflow structure and unfavorable thermodynamic conditions, thus leading to improved intensity forecasts.

1. Introduction

In contrast to the significant improvements in tropical cyclone (TC) track forecasts, only limited progress has been made in TC intensity forecasting in the last two decades (Rogers et al. 2006, 2013; Rappaport et al. 2009; Gall et al. 2013). Part of the difficulty in forecasting the intensity of TCs originates from deficiencies in the representation of the initial vortices in numerical weather prediction (NWP) models due to the general lack of high-resolution observations within the TC inner-core region (Pu and Braun 2001; Pu et al. 2009; Zhang et al. 2011). Recently, observations of the TC inner-core region and its near environment, obtained via tail Doppler radar (TDR) data and dropwindsonde observations that have

been collected by National Oceanic and Atmospheric Administration (NOAA) aircraft reconnaissance missions, have made their way into NWP systems and have contributed toward significant improvements in Atlantic TC intensity forecasting (Rogers et al. 2006, 2013; Zhang et al. 2011; Gall et al. 2013; Pu et al. 2016). However, outside the Atlantic basin, these airborne Doppler radars and dropwindsonde data are not routinely available. Even in the Atlantic, there can be large temporal gaps in data collection in the TC inner-core region.

Because of the lack of routine radar and aircraft dropwindsonde observations over the ocean from reconnaissance missions, satellite radiances and satellite-derived products are important data sources for use in operational data assimilation. Unfortunately, limitations of current data assimilation methodologies prevent most satellite radiances in the TC inner core and near

Corresponding author: Dr. Zhaoxia Pu, zhaoxia.pu@utah.edu

DOI: 10.1175/MWR-D-17-0136.1

© 2018 American Meteorological Society. For information regarding reuse of this content and general copyright information, consult the [AMS Copyright Policy](http://www.ametsoc.org/PUBSReuseLicenses) (www.ametsoc.org/PUBSReuseLicenses).

environmental regions from being assimilated. This occurs because of cloud and precipitation contamination, although all-sky data assimilation has become an active research area in recent years (Zhu et al. 2016). Fortunately, satellite-derived products, especially atmospheric motion vectors (AMVs; Velden et al. 1997, 2005) derived from geostationary satellites, have supplied useful information for improving hurricane forecasting. Previous studies have demonstrated that assimilating these AMVs into NWP models can result in improved analyses and forecasts of TCs and their environment. Langland et al. (2009) and Berger et al. (2011) found that track forecasts in the Navy Operational Global Atmospheric Prediction System (NOGAPS) were improved, owing to the more accurate representation of the environmental flow when AMVs were assimilated. Soden et al. (2001) demonstrated that the assimilation of AMVs led to a more accurate representation of the steering flow, thus improving TC track forecasts in the Geophysical Fluid Dynamics Laboratory (GFDL) hurricane model. Pu et al. (2008) also found that the assimilation of *GOES-II* rapid scan AMVs has a positive impact on numerical forecasts of TC intensity and precipitation.

More recently, upgraded AMV processing algorithms and strategies have enabled improvements in the coverage, density, and quality of AMVs. These “enhanced” AMV datasets can better capture smaller-scale wind flows and provide information on TC-scale flow fields (Velden et al. 2017). Wu et al. (2014, 2015) used an ensemble Kalman filter method to assimilate enhanced AMV data into the mesoscale community Weather Research and Forecasting (WRF) Model. They found that initial analyses of TC vortex location, intensity, and structure are all improved, along with subsequent forecasts, due to the assimilation of enhanced AMVs. Furthermore, Velden et al. (2017) incorporated enhanced AMVs into the National Centers for Environmental Prediction (NCEP) Hurricane WRF (HWRF) Model. They found an overall modest positive impact of enhanced AMVs on HWRF forecasts, but suggested that the degree of the impact may be limited by the vortex initialization procedure used.

Although all of the above studies demonstrate that enhanced AMVs are useful for improving the numerical prediction of TCs, most of these studies incorporate the enhanced AMVs into only the storm environment region (viz., the outer model domains with coarser resolution that mainly resolves the large-scale environment information around TCs) instead of the TC inner-core region (i.e., the innermost model domain with the finest resolution that mainly resolves TC inner core and its immediate vicinity). Therefore, optimal data assimilation (DA) approaches to promote the impacts of enhanced

inner-core AMVs to improve model intensity forecasts have not yet been examined. Considering the emerging availability of operational high temporal (5–15 min) and spatial (~15–25 km) resolution enhanced AMVs, it is essential to investigate the potential impacts on hurricane vortex initialization and intensity forecasts. Moreover, satellite-derived observations, such as enhanced AMVs, are now being assimilated in the operational NCEP HWRF (Tallapragada et al. 2015). However, the TC inner-core AMV increments are not used in favor of a separate vortex initialization (VI) procedure. It is our goal to use a research version of the HWRF Model and the NCEP Gridpoint Statistical Interpolation analysis system (GSI)-based ensemble–variation hybrid DA system to further examine the potential impacts of assimilating enhanced AMVs on the HWRF analyses and forecasts, especially mature hurricanes. Specifically, we will evaluate two different DA strategies—a method that is similar to the current operational approach, in which VI is performed before all other data are assimilated, and an exploratory method that uses the same HWRF DA configuration but omits the use of VI. Two hurricane cases that had notable intensity changes during their life cycles are examined.

An introduction of the HWRF Model and the DA system and descriptions of the hurricane case studies are presented in section 2. The experiment design and the impacts of enhanced AMV DA on track and intensity forecasts are discussed in section 3. Section 4 demonstrates the improvements in initial conditions and the changes in analyzed and forecasted storm structures due to the assimilation of enhanced AMVs and their sensitivities to the different DA strategies. A summary and discussion are given in section 5.

2. HWRF Model, hurricane cases, and experimental design

a. HWRF Model and initialization

The NCEP HWRF Model (Gopalakrishnan et al. 2011; Bao et al. 2012), version 3.7a (HWRFv3.7a), is used in this study. In brief, the model grid setup and physics options are configured as closely as possible to the 2015 operational HWRF (Tallapragada et al. 2015). The dynamical core used in HWRF is the same as that used in NCEP’s WRF-Nonhydrostatic Mesoscale Model (NMM; Janjić et al. 2010). In HWRFv3.7a, the NMM core is configured with three domains (d01, d02, and d03) with domain sizes of 5900 km × 5900 km, 1500 km × 1500 km, and 800 km × 800 km (see Fig. 1) and grid spacings of 18, 6, and 2 km, respectively. A suite of advanced physical parameterizations developed for

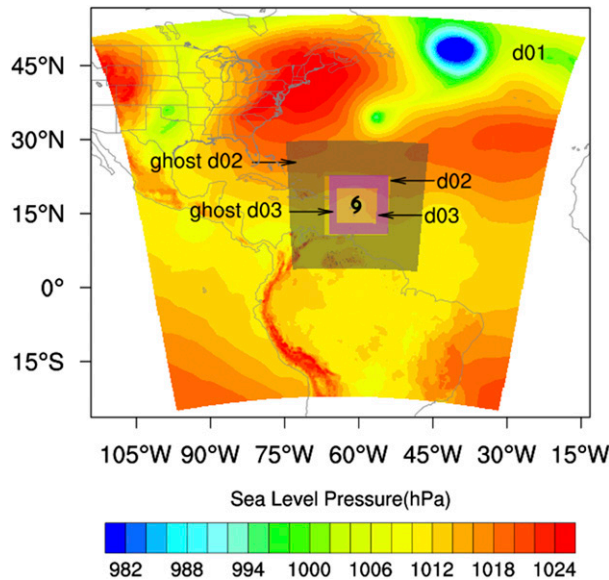


FIG. 1. HWRf-simulated sea level pressure (color contours, units hPa) and storm center from NHC best track (black storm sign) at 0600 UTC 13 Oct 2014 for Hurricane Gonzalo. HWRf Model forecast domains, as indicated by d01, d02, and d03 labels, and HWRf DA domains, as indicated by ghost d02 (black shaded area) and ghost d03 (pink shaded area), are also indicated. The black hurricane symbol indicates the storm center at the time.

TC applications is employed. This includes the modified GFDL surface-layer parameterization (e.g., Powell et al. 2003; Black et al. 2007; Kwon et al. 2010), the Noah land surface model (e.g., Chen and Dudhia 2001; Mitchell et al. 2005), the modified Rapid Radiative Transfer Model for general circulation models (RRTMG) shortwave and longwave radiation scheme (e.g., Iacono et al. 2008), the Ferrier–Aligo microphysical parameterization (e.g., Ferrier et al. 2002; Ferrier 2005; Aligo et al. 2014), the Global Forecast System (GFS) planetary boundary layer (PBL) scheme (e.g., Hong and Pan 1996), and the GFS simplified Arakawa–Schubert (SAS) cumulus scheme (e.g., Han and Pan 2011). The cumulus parameterization is active only in the 18- and 6-km grid-spacing domains.

The HWRf initialization adopts a combination of VI with the NCEP GSI-based ensemble three-dimensional variational hybrid data assimilation system (hereafter “GSI-3DEnVar hybrid DA system”; Wu et al. 2002; Wang et al. 2013). In this study, we refer to this procedure as “DA with VI.” The VI scheme (Liu et al. 2006) performs the relocation, resizing, and intensity correction on the vortex using the National Hurricane Center (NHC) tropical cyclone vital statistics (TCVitals) database in order to correct the storm position and intensity to approach the real-time estimation [see details in Tallapragada et al. (2015)].

After VI, observations are assimilated by the GSI-3DEnVar hybrid DA system to further improve the initial conditions for the HWRf forecast. DA is performed on two large domains that are referred to as ghost d02 (~6-km grid spacing) and ghost d03 (~2-km grid spacing). Note that ghost d02 (ghost d03) covers the corresponding d02 (d03) domain as shown in Fig. 1, but ghost d02 (about 3000 km × 3000 km) and ghost d03 (about 1600 km × 1600 km) are larger than d02 and d03. Similar to the 2015 operational settings but without the ocean coupling, which is referred to as the control experiment in this study, all conventional and satellite observations are assimilated in ghost d02, while only conventional observations and TDR data are assimilated in ghost d03. After the GSI data assimilation, the analyses on ghost d02 and ghost d03 are interpolated back into the d02 and d03 domains, meaning that the data assimilation still takes effect on d02 and d03. In addition, outcomes from d02 and d03 generated by the above processes are also merged into the outermost domain (d01), in which the initial conditions are directly downscaled from the GFS analysis, to refine the vortex and storm-environment information in d01. Finally, these results in d01, d02, and d03 provide initial conditions for the HWRf forecast. It should be noted that the merging procedure also blends the analysis field from GSI with the first guess from VI, based on the horizontal and vertical positions of model grid points. The source of the final initial conditions for the HWRf forecast varies with the distance to the storm center and the model vertical levels, as listed in Table 1.

It has been proven that “DA with VI” results in significant improvements in NCEP operational hurricane forecasting with the HWRf Model. However, in some cases, VI and DA can counteract each other (Tallapragada et al. 2015). Meanwhile, VI may also induce gradient imbalances in the initial vortex of a mature hurricane and lead to vortex spin-down at the beginning of the HWRf forecast (e.g., Tong et al. 2014; Pu et al. 2016). Because of this, impacts from DA could be difficult to see clearly in some cases. To better understand the impacts of the enhanced AMVs on HWRf forecasts, an additional configuration of the initialization procedure for HWRf, referred to as “DA without VI,” is also examined in this study. In “DA without VI,” the VI is completely turned off. Neither TC relocation nor intensity corrections are performed. Because of the application restriction, the data assimilation in “DA without VI” is directly performed on d01, d02, and d03. Specifically, the conventional, all other satellite observations, and enhanced AMVs are assimilated in d01 and d02 (storm environment region), while only conventional observations and enhanced AMVs are assimilated

TABLE 1. Source of the final initial conditions for the HWRF forecast after the merging procedure. The top row represents the model vertical levels, and the first column represents the distance to the storm center.

	>600 hPa	600–400 hPa	<400 hPa
<150 km	First guess	Blend analysis field with first guess	Analysis field
150–300 km	Blend analysis field with first guess	Blend analysis field with first guess	Blend analysis field with first guess
>300 km	Analysis field	Analysis field	Analysis field

in d03 (storm inner-core region and its immediate vicinity; “inner-core” hereafter). As indicated in the previous paragraph, the data assimilation takes effect mainly on d02 (d03) in the VI with DA, even if the data assimilation is performed on ghost d02 (ghost d03).

Background error covariance in the GSI-3DEnVar hybrid DA system is a combination of the static background error covariance generated by the National Meteorological Center (NMC) method (Parrish and Derber 1992; Wu et al. 2002; Kleist et al. 2009) and a flow-dependent background error covariance derived from the ensemble forecasts (Wang et al. 2013). The weighting factor for static and flow-dependent error covariance is set to 0.2 and 0.8, respectively, meaning more weight is given to the ensemble background. In this study, the flow-dependent background error covariance is generated from the NCEP operational GFS 80-member ensemble forecast at a resolution of T574 (~23 km) for all experiments.

b. Hurricane cases and observations

Hurricanes Gonzalo (2014) and Joaquin (2015) are selected as study cases. Detailed descriptions of these two cases can be found in Brown (2014) and Berg (2016). Specifically, the intensification periods from 0000 UTC 13 October to 1800 UTC 16 October 2014 for Hurricane Gonzalo and from 1800 UTC 27 September to 0600 UTC 2 October 2015 for Hurricane Joaquin are emphasized in this study. However, two other intensity change periods—the reintensification period from 1800 UTC 1 October to 1800 UTC 3 October and the rapid weakening phase from 1800 UTC 2 October to 1800 UTC 6 October 2015—for Hurricane Joaquin are also analyzed.

The HWRF GSI-3DEnVar hybrid DA system assimilates the NCEP operational satellite and conventional observations (these are included in the NCEP prepbuf files), including the satellite-derived winds, here referred to as the operational AMVs, but not the enhanced AMV datasets considered in our study. A list of satellite and conventional data types for operational HWRF can be found on the NCEP website (http://www.emc.ncep.noaa.gov/mmb/data_processing/prepbuf.doc/table_2.htm and

[table18.htm](#)). Also, NOAA P3 TDR radial winds are assimilated in the current operational HWRF when they are available. Unfortunately, TDR data are not available during the data assimilation periods for the two hurricane cases in this study (Table 2). Figure 2 illustrates the spatial and vertical distribution of all observations except for satellite radiances within a 6-h window assimilated by the GSI DA system at 1800 UTC 13 October 2014 for Hurricane Gonzalo and at 0600 UTC 29 September 2015 for Hurricane Joaquin. It is apparent that the observations are sparse both horizontally and vertically, especially in the area around the storm centers (within <600 km of the radius; Figs. 2a–d). The operational AMVs represent most of the conventional observations available for the DA for these two hurricanes. In addition, the observations are denser around Joaquin than around Gonzalo (Figs. 2a,c). The vertical distribution also reveals that observations in the midtroposphere (700–400 hPa) and boundary layer (below 800 hPa) are much sparser than those in the upper levels (above 400 hPa) in both cases (Figs. 2b,d). The lack of enhanced AMVs in the midlevel (700–400 hPa) is determined by the nature of the retrieval algorithm. Since the typical vertical distribution of AMVs in the tropics is highly bimodal (cirrus level and marine cumulus level) and the retrieved AMVs show higher vector errors between 700 and 400 hPa (Sears and Velden 2012; Velden et al. 2017), the AMVs in this height range were excluded from the data-processing period. Similar characteristics of data distribution are found in other analysis cycles (figures not shown).

c. Enhanced AMVs

The novel dataset being assimilated in this study is the enhanced AMVs processed and provided by the Cooperative Institute for Meteorological Satellite Studies (CIMSS), University of Wisconsin. These datasets are derived from GOES data and are part of a demonstration for applications to advanced geosatellite imagers now becoming operational (GOES-R/S, *Himawari-8/9*). The enhanced AMVs are quality controlled before being entered into the HWRF GSI; enhanced AMVs are assimilated only if the quality indicator (QI) is equal to or larger than an empirically determined value of 0.6

TABLE 2. List of DA experiments performed on Hurricane Gonzalo (2014) and Hurricane Joaquin (2015).

Expt	VI in DA	DA period	DA domains and data
VI-CTRL	Yes	Hurricane Gonzalo: 0000–1800 UTC 13 Oct 2014	ghostd02: Conventional observations, satellite observations ghostd03: Conventional observations
		Hurricane Joaquin: 0000 UTC 28 Oct–0600 UTC 29 Oct 2015	
		Hurricane Joaquin: 0000–1800 UTC 2 Oct 2015	
		Hurricane Joaquin: 1800 UTC 2 Oct–1800 UTC 3 Oct 2015	
VI-NIN-AMV	Yes	Hurricane Gonzalo: 0000–1800 UTC 13 Oct 2014	ghostd02: Conventional observations, satellite observations, enhanced AMVs ghostd03: Conventional observations
		Hurricane Joaquin: 0000 UTC 28 Oct–0600 UTC 29 Oct 2015	
		Hurricane Joaquin: 0000–1800 UTC 2 Oct 2015	
		Hurricane Joaquin: 1800 UTC 2 Oct–1800 UTC 3 Oct 2015	
VI-AMV	Yes	Hurricane Gonzalo: 0000–1800 UTC 13 Oct 2014	ghostd02: Conventional observations, satellite observations, enhanced AMVs ghostd03: Conventional observations, enhanced AMVs
		Hurricane Joaquin: 0000 UTC 28 Oct–0600 UTC 29 Oct 2015	
		Hurricane Joaquin: 0000–1800 UTC 2 Oct 2015	
		Hurricane Joaquin: 1800 UTC 2 Oct–1800 UTC 3 Oct 2015	
NVI-CTRL	No	Hurricane Gonzalo: 0000–1800 UTC 13 Oct 2014	d01, d02: Conventional observations, satellite observations d03: Conventional observations
		Hurricane Joaquin: 0000 UTC 28 Oct–0600 UTC 29 Oct 2015	
		Hurricane Joaquin: 0000–1800 UTC 2 Oct 2015	
		Hurricane Joaquin: 1800 UTC 2 Oct–1800 UTC 3 Oct 2015	
NVI-NIN-AMV	No	Hurricane Gonzalo: 0000–1800 UTC 13 Oct 2014	d01, d02: Conventional observations, satellite observations, enhanced AMVs d03: Conventional observations
		Hurricane Joaquin: 0000 UTC 28 Oct–0600 UTC 29 Oct 2015	
		Hurricane Joaquin: 0000–1800 UTC 2 Oct 2015	
		Hurricane Joaquin: 1800 UTC 2 Oct–1800 UTC 3 Oct 2015	
NVI-AMV	No	Hurricane Gonzalo: 0000–1800 UTC 13 Oct 2014	d01, d02: Conventional observations, satellite observations, enhanced AMVs d03: Conventional observations, enhanced AMVs
		Hurricane Joaquin: 0000 UTC 28 Oct–0600 UTC 29 Oct 2015	
		Hurricane Joaquin: 0000–1800 UTC 2 Oct 2015	
		Hurricane Joaquin: 1800 UTC 2 Oct–1800 UTC 3 Oct 2015	

(Wu et al. 2014). In addition, enhanced AMVs meeting these QI thresholds but with expected error (EE) values of $>4.5 \text{ m s}^{-1}$ are filtered out, unless the AMV is $>25 \text{ m s}^{-1}$ and has an attending QI > 0.7 . The QI and EE values are produced during the AMV derivation process and represent internal quality control (QC) indicators of AMV quality (Velden et al. 2017). In addition to the QC, data thinning is also performed on enhanced AMVs using the method embedded in GSI (see details in the GSI users' guide, available at http://www.dtcenter.org/com-GSI/users/docs/users_guide/GSIUserGuide_v3.5.pdf). Specifically, the horizontal thinning grid size for enhanced AMVs is 6 km, the same as the horizontal grid spacing of HWRF d02 and ghost d02 (see Fig. 1). This scale is used to incorporate the storm-scale information carried by the enhanced AMVs and data into the HWRF initial conditions, as well as to reveal the advantage of high-resolution coverage of enhanced AMVs.

Figures 3a and 3b show the horizontal distribution of operational AMVs and enhanced AMVs assimilated by HWRF GSI at 1800 UTC 13 October 2014 for Hurricane Gonzalo. The operational AMVs are produced at 6-h intervals, while enhanced AMVs are produced at hourly intervals, and all AMVs within a 6-h window ($\pm 3 \text{ h}$ of the analysis time) are included. In contrast to the sparse distribution of operational AMVs (Fig. 3a), the denser coverage of enhanced AMVs blankets the storms and their

environment (Fig. 3b). The blue rectangular block of very dense low-level vector coverage in Fig. 3b is due to the availability of rapid scan images from GOES-East at this time. The more frequent imaging (~ 7 -min scans) promotes denser vector coverage. In addition, the radial pressure distribution further shows that enhanced AMVs also improve the vertical data coverage in the upper layers (above 400 hPa) and boundary layers (below 700 hPa) of Hurricane Gonzalo. Particularly, the lack of observations within a 300–900-km radius of the storm center, as shown in Fig. 2b, is significantly improved (Fig. 3c). Similar characteristics of the operational AMVs and enhanced AMVs are also observed for Hurricane Joaquin (Figs. 3d–f), except that the operational AMVs for Hurricane Joaquin have a much denser distribution (Fig. 3d) than in Fig. 3a, with data coverage enhanced mainly in the lower troposphere (below 700 hPa) (Figs. 3e,f). Moreover, a comparison of Fig. 3b and Fig. 3e shows that the enhanced AMVs are dominant in the upper level (within 400 km of the storm center) for Hurricane Gonzalo (Fig. 2a) but are denser in the lower (upper) levels in the north (south) quadrants for Hurricane Joaquin (Fig. 2b), indicating the different cloud structures and outflow configurations in the two storms at these times. Overall, the enhanced AMVs can significantly improve the horizontal and vertical data coverage for Hurricanes Joaquin and Gonzalo, especially around the storm center (< 900 -km radius). As will be

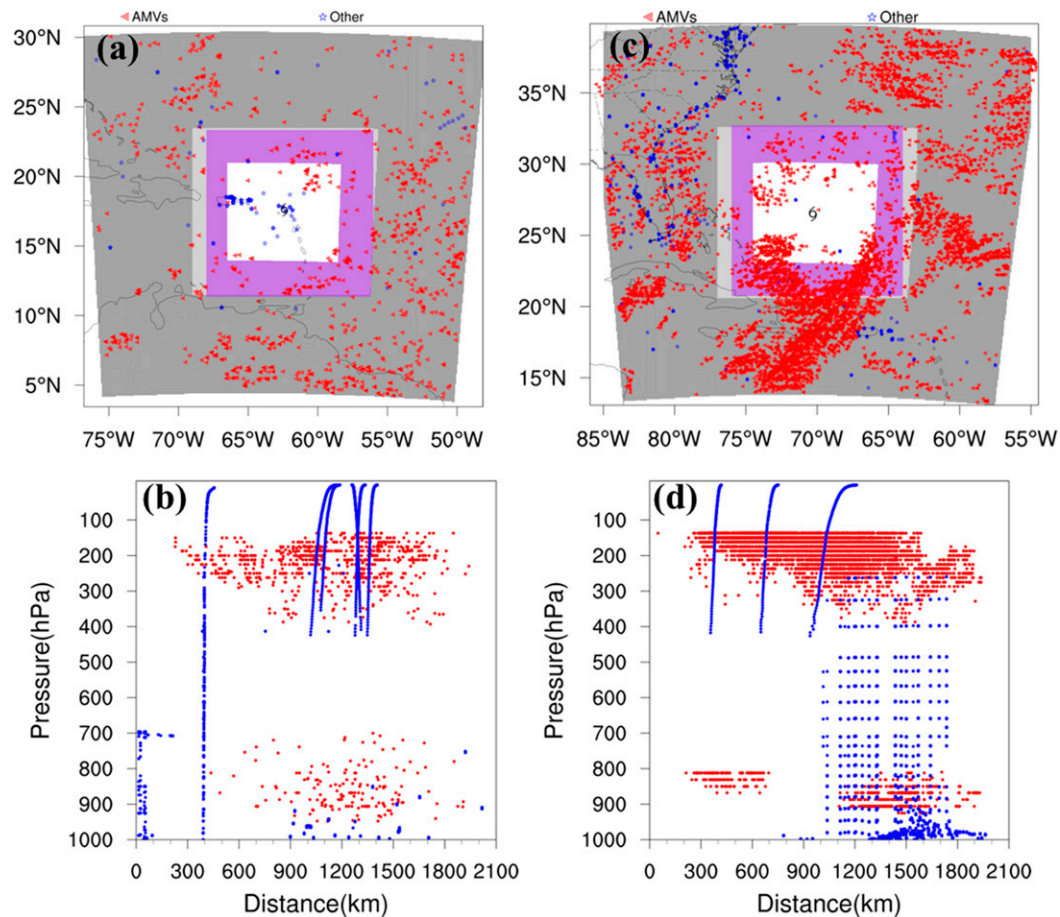


FIG. 2. Spatial distribution of all observations, except for satellite radiances, assimilated by the GSI DA system at (a) 1800 UTC 13 Oct 2014 for Hurricane Gonzalo and (c) 0600 UTC 29 Sep 2015 for Hurricane Joaquin. The observations are grouped into two types: operational AMVs (red) and all other observations (blue). The shaded areas indicate the ghost d02 (black shaded area), ghost d03 (pink shaded area), d02 (light gray shaded area), and d03 (white color area) domains, corresponding to Fig. 1. (b),(d) Radius–pressure distributions corresponding to observations as shown in (a),(c).

discussed later, the enhanced data coverage around the storm center from the enhanced AMVs will have a substantial contribution to the HWRf forecasts of these two hurricanes.

3. Data assimilation experiments and results

a. Hurricane Gonzalo

For Hurricane Gonzalo, the HWRf Model is initialized at 1800 UTC 12 October 2014 and spins up until 0000 UTC 13 October 2014. Then, the 6-hourly DA and forecast cycles are performed from 0000 to 1800 UTC 13 October 2014 to reach the intensification phase. A 72-h forecast from 1800 UTC 13 October to 1800 UTC 16 October 2014 is then performed to predict intensity changes of Hurricane Gonzalo. The

first group of experiments (VI experiments) is based on “DA with VI.” A combination of VI with DA is used in each analysis cycle. A set of three DA experiments is performed for Hurricane Gonzalo to examine the effects of incorporating the enhanced AMVs into one or both ghost domains. Details of the experimental design are listed in Table 2.

The track and intensity forecasts from the HWRf simulations are compared against the NHC best track data. Figure 4 shows the time series of track and intensity in terms of minimum sea level pressure (MSLP) and maximum surface wind (MSW) during the 72-h forecast for Hurricane Gonzalo. The track errors in all experiments are similar and small (e.g., within 50 km) over the 72-h forecasts (Fig. 4a). A notable unrealistic weakening is found in the intensity forecast of Hurricane Gonzalo in terms of both MSLP (Fig. 4b) and MSW

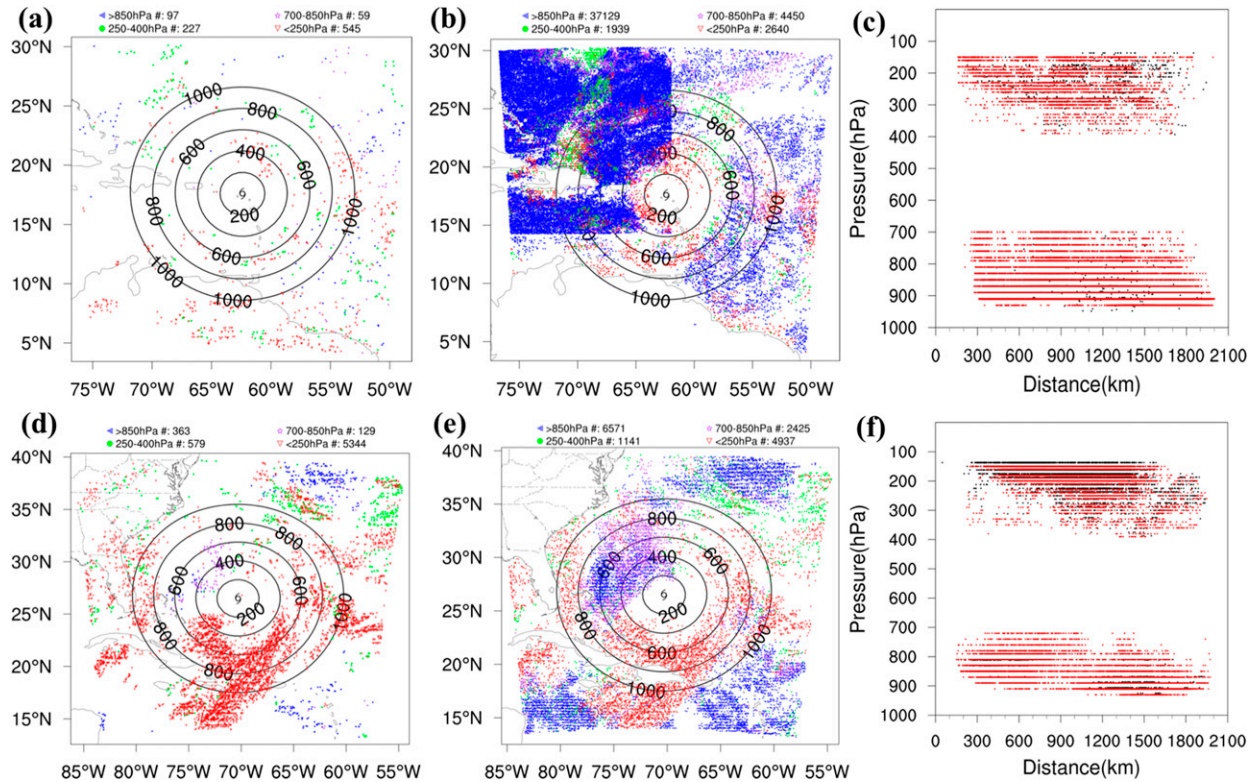


FIG. 3. Spatial distribution of (a) operational AMVs and (b) enhanced AMVs in ghost d02 assimilated by GSI DA system at 1800 UTC 13 Oct 2014 for Hurricane Gonzalo. The AMVs are grouped into four layers, <250 hPa (red), 250–400 hPa (green), 700–850 hPa (purple), and >850 hPa (blue), by their assigned heights and are shown by the corresponding colors, with numbers indicating the total number of AMVs in each grouped layer. There are no enhanced AMV observations between 400 and 700 hPa. (c) The radius–pressure distribution of operational AMVs (black dots) and enhanced AMVs (red dots) as shown in (a),(b). (d)–(f) As in (a)–(c), but for Hurricane Joaquin at 0600 UTC 29 Sep 2015.

(Fig. 4c) after the first 6-h forecast (until 0000 UTC 14 October 2014) in the VI-CTRL simulation (no enhanced AMVs). As a result, the intensity forecast is significantly degraded, leading to an average MSLP error of 15.4 hPa and an average MSW error of 18.6 m s^{-1} over the 72-h forecasts. The assimilation of enhanced AMVs leads to significant improvements in the intensity forecasts. Specifically, the unrealistic vortex weakening after the first 6-h forecast still exists in the VI-NIN-AMV simulation (AMVs only assimilated only in the d02 domain); however, the averaged MSLP (MSW) error over the 72-h forecast is reduced by 50% (35%), compared with that in VI-CTRL (Figs. 4b,c). With the assimilation of enhanced AMVs to also include the innermost domain (d03) in VI-AMV, the unrealistic vortex weakening after the first 6-h forecast is eliminated, and significant improvements in the intensity forecasts of Hurricane Gonzalo are evident: the average error of MSLP (MSW) over the 72-h forecasts in VI-AMV is reduced by about 80% (40%), compared with that in VI-CTRL (Figs. 4b,c).

Corresponding to the “DA with VI” experiments, a set of three “DA without VI” experiments is also performed for Hurricane Gonzalo (see details in Table 2). Figure 5 shows the track and intensity forecasts from the NVI experiments. It is apparent that the assimilation of enhanced AMVs leads to positive impacts on both track and intensity forecasts. Notably, the extent of the impacts depends on whether the enhanced AMVs are assimilated in the inner-core region or not. As shown in Fig. 5a, the assimilation of enhanced AMVs leads to a reduction of average track errors over the 36-h forecast by 9% in NVI-NIN-AMV (52 km) and by 18% in NVI-AMV (46 km), compared to that in NVI-CTRL (56 km). The average MSLP (MSW) forecast error over the 72-h forecasts is reduced by 12% (15%) in NVI-NIN-AMV and by 42% (20%) in NVI-AMV (Figs. 5b,c).

b. Hurricane Joaquin

Similar to Hurricane Gonzalo, experiments are also conducted for the intensification period of Hurricane Joaquin. Specifically, the model is initialized at 1800

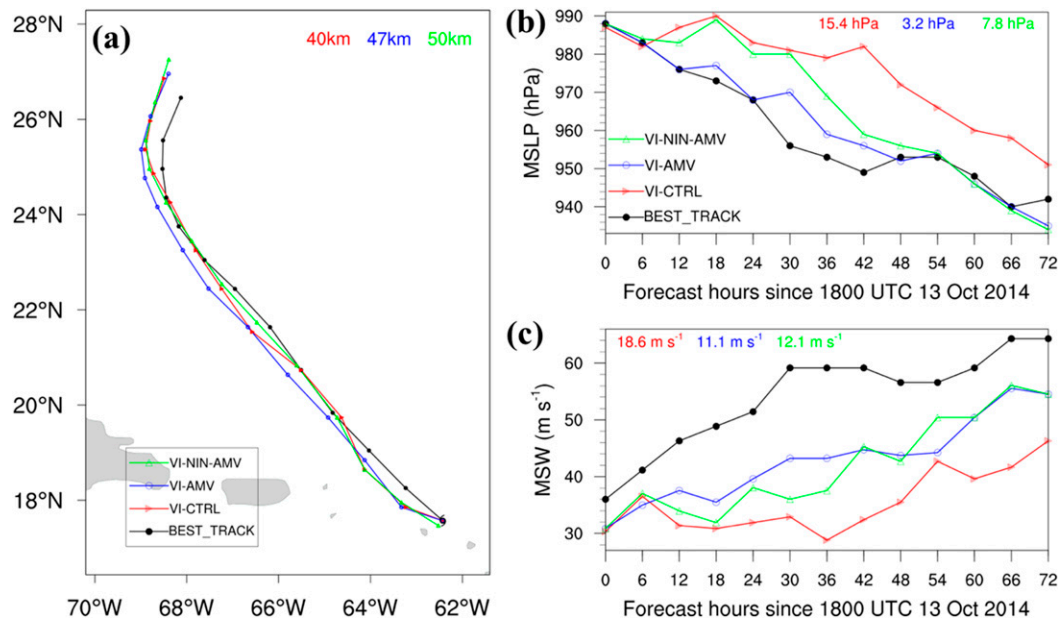


FIG. 4. The 72-h HWRf forecast from 1800 UTC 13 Oct 2014 for Hurricane Gonzalo of (a) track and intensity in terms of (b) minimum MSLP (hPa) and (c) maximum surface wind (m s^{-1}) from VI-CTRL (red lines), VI-AMV (blue lines), and VI-NIN-AMV (green lines). The track, MSLP, and MSW are verified against NHC best track data (black lines). The colored numbers in (c) denote the averaged track errors and absolute intensity errors for the corresponding experiments as indicated in (b).

UTC 27 September 2015 and allowed to spin up to 0000 UTC 28 September 2015, and the cycled DA is performed from 0000 UTC 28 September to 0600 UTC 29 September 2015 in 6-h windows. Then, a 72-h forecast from 0600 UTC 29 September to 0600 UTC 2 October 2015 is performed to simulate the intensification period of Hurricane Joaquin. A set of three DA experiments is performed for “DA with VI” and “DA without VI” (see details in Table 2). Figure 6 illustrates the track and intensity forecast over a 72-h forecast for the “DA with VI” experiments for the intensification phase of Hurricane Joaquin. As shown in Fig. 6a, large average track errors over the 48-h forecast are present in the VI-CTRL, VI-NIN-AMV, and VI-AMV experiments (150, 163, and 133 km, respectively). However, VI-AMV saw a 10% reduction in track errors, compared with VI-CTRL, indicating that the assimilation of enhanced AMVs in the inner-core region may also improve the track forecast in some cases. After 48 h, the track forecasts in all simulations have totally drifted away from the best track. Because of large track errors in all experiments, the intensity forecasts for Hurricane Joaquin lose their significance, although all the HWRf forecasts captured the intensity changes of Hurricane Joaquin during the period from 0600 UTC 29 September to 0600 UTC 2 October 2015 (Figs. 6b,c). In addition, the assimilation of enhanced AMVs leads to positive impacts on the MSW forecasts of Hurricane Joaquin, as VI-NIN-AMV

and VI-AMV lead to a reduction in the average error of MSW by $\sim 20\%$ relative to VI-CTRL (Fig. 6c).

For the “DA without VI” experiments, the initial track deviates from the best track since VI is turned off during the DA period, leading to large track errors at the initial time in all three experiments (Fig. 7a) during the intensification phase of Hurricane Joaquin. The assimilation of enhanced AMVs in the parent and intermediate domains (NVI-NIN-AMV) has little to no impact on either track or intensity forecasts, as compared with that in NVI-CTRL. In contrast, the assimilation of enhanced AMVs (NVI-AMV) to the innermost domain leads to significant improvements in both track and intensity forecasts: the average track error over the 48-h forecasts in NVI-AMV is decreased by 43%, compared to that in NVI-CTRL (Figs. 7b,c). Also notable is that the forecasted track in NVI-AMV moves southwest in the first 48-h forecast, which captures the actual trend in the NHC best track. The average intensity errors of both MSLP and MSW over the 72-h forecasts in NVI-AMV are decreased by about 70%, compared to those in NVI-CTRL (Figs. 7b,c).

Note that the track forecast errors are large in all above experiments during the intensification period of Hurricane Joaquin. In fact, as revealed by most of the operational models during the real-time forecasting, the track forecast during the intensification stage of

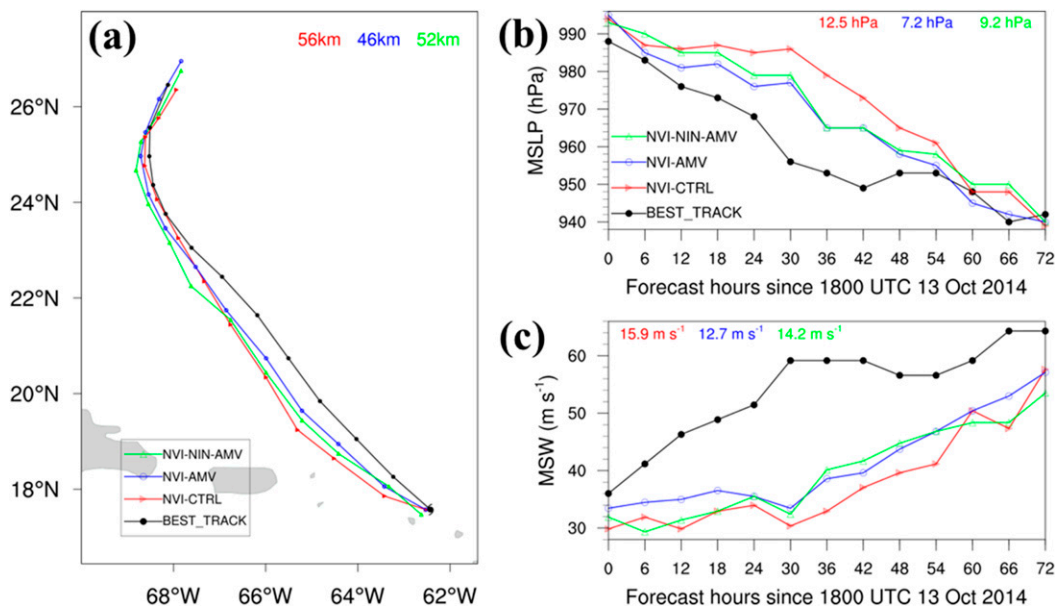


FIG. 5. As in Fig. 4, but for the 72-h HWRf forecast from NVI-CTRL (red lines), NVI-AMV (blue lines), and NVI-NIN-AMV (green lines) for Hurricane Gonzalo during the period from 1800 UTC 13 Oct to 1800 UTC 16 Oct 2014.

Hurricane Joaquin is difficult to capture (Berg 2016). However, it is hard to evaluate the contribution of DA to the hurricane forecast, as the large track errors can envelop the data impact very quickly. To generalize the conclusion for the impact of enhanced AMVs on Hurricane Joaquin, two additional sets of experiments are performed. First, the HWRf Model is initialized at 1800 UTC 1 October 2015 and allowed to spin up to 0000 UTC 2 October 2015, and the cycled DA is performed from 0000 to 1800 UTC 2 October 2015 in 6-h windows.

Then, a 72-h forecast from 1800 UTC 2 October to 1800 UTC 5 October 2015 is performed to simulate the re-intensification phase of Hurricane Joaquin. Second, the HWRf Model is initialized at 1800 UTC 2 October 2015 and allowed to spin up to 0000 UTC 3 October 2015, and the cycled DA is performed from 0000 to 1800 UTC 3 October 2015 in 6-h windows. Then, a 72-h forecast from 1800 UTC 3 October to 1800 UTC 6 October 2015 is performed to simulate the mature phase of Hurricane Joaquin. A set of six experiments (three for “DA

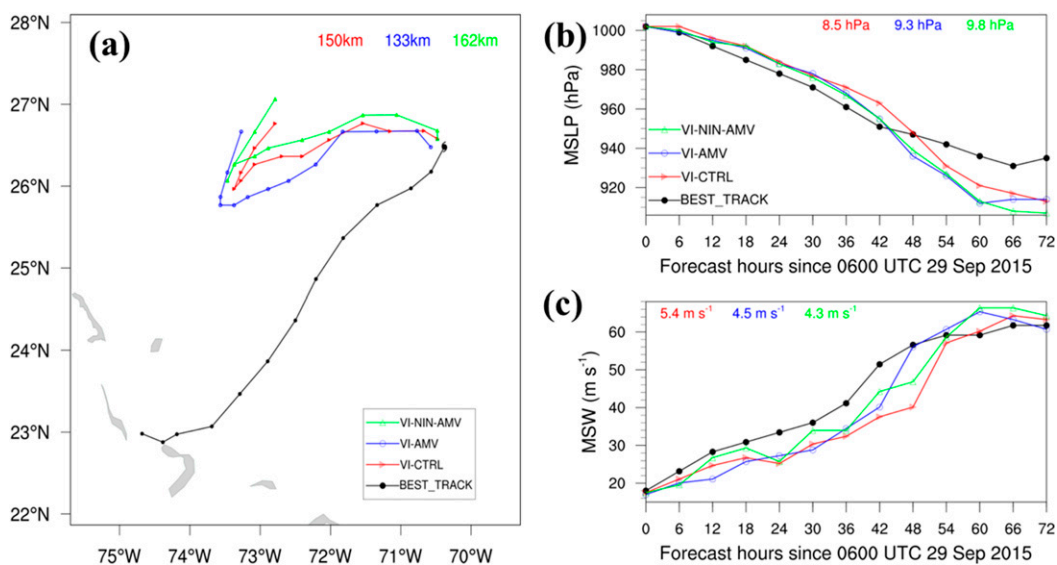


FIG. 6. As in Fig. 4, but for the 72-h HWRf forecast from VI-CTRL (red lines), VI-AMV (blue lines), and VI-NIN-AMV (green lines) for Hurricane Joaquin during the period from 0600 UTC 29 Sep to 0600 UTC 2 Oct 2015.

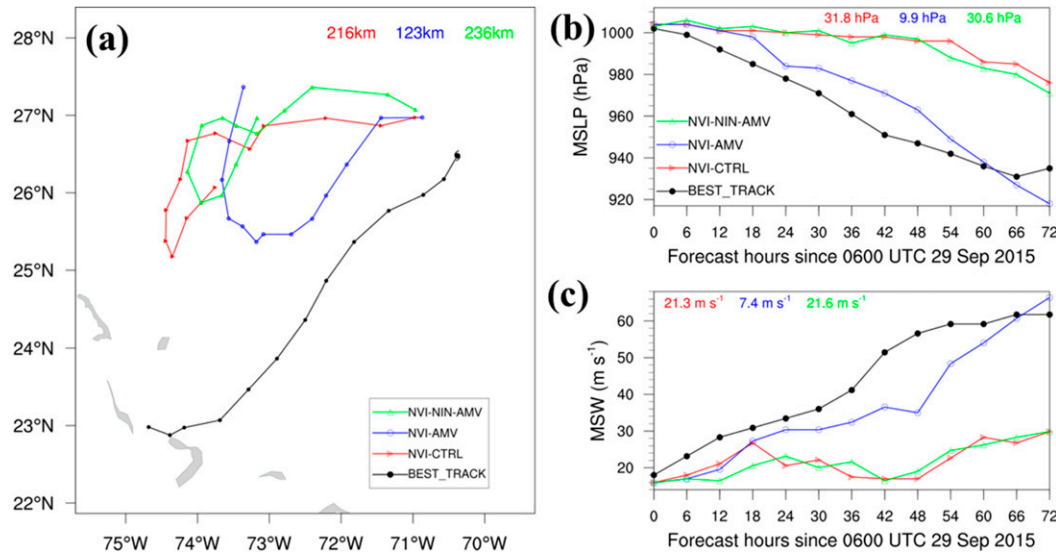


FIG. 7. As in Fig. 4, but for the 72-h HWRf forecast from NVI-CTRL (red lines), NVI-AMV (blue lines), and NVI-NIN-AMV (green lines) for Hurricane Joaquin during the period from 0600 UTC 29 Sep to 0600 UTC 2 Oct 2015.

with VI” and three for “DA without VI”) is performed for the reintensify phase/rapid weakening phase of Hurricane Joaquin (see Table 2 for detailed configurations for each experiment).

Figures 8 and 9 show the 72-h track and intensity forecasts for the reintensification and rapid weakening phases of Hurricane Joaquin. For the track forecast in the reintensification phase (Figs. 8a,d), the overall average track errors over the 72-h forecast in VI-CTRL (NVI-CTRL), VI-NIN-AMV (NVI-NIN-AMV), and VI-AMV (NVI-AMV) are 135 (75), 105 (80), and 75 (75) km, respectively. This suggests that the assimilation of enhanced AMVs improves the track forecasts in “DA with VI” experiments, especially when the data are assimilated in the inner-core region, although this is not true in “DA without VI.” For the track forecast in the rapid weakening phase, the assimilation of enhanced AMVs seems to slightly degrade the track forecast (except for VI-AMV) due to the large track errors after 48-h forecast from the perspective of average track errors (colored numbers in Figs. 9a,d). However, the track forecasts in all the simulations are not distinguishable during the first 48-h forecast, and the track forecasts in all simulations nearly match the best track forecast.

The mixing impacts of enhanced AMVs on the MSLP and MSW are observed during the reintensification and rapid weakening phases of Hurricane Joaquin (Figs. 8b,c,e,f, 9b–f). In addition, the “DA without VI” can cause large initial errors for MSW (Figs. 8f, 9f), indicating that the enhanced AMVs data only are not enough to force the storm intensity to match the observed intensity for this case. However, it is worth noting that the assimilation of enhanced AMVs in the

inner-core region produces smaller average MSLP and MSW errors over the whole 72-h forecasts in most of the cases (e.g., the blue numbers at the top of each panel in Figs. 8b,c, 8e,f, and 9b,c are always smaller than the red and green numbers). Overall, the above results suggest that the inner-core DA of enhanced AMVs can strengthen the positive impact of AMVs on HWRf intensity forecast, especially in operational scenarios (“DA with VI”).

c. Discussion on the impact of enhanced AMVs

Although the results from “DA with VI” and “DA without VI” experiments may not be directly compared since they were configured differently, the assimilation of enhanced AMVs leads to positive impacts on track and intensity forecasts of Hurricanes Gonzalo and Joaquin when comparing the results from three simulations in each of configuration. The degrees of the impacts depend on the DA configuration used and vary with the hurricane cases. Also, among the three simulations in “DA with VI” (“DA without VI”), the VI-AMV (NVI-AMV) with assimilation of enhanced AMVs in the inner-core region leads to overall better intensity forecasts than VI-CTRL and VI-NIN-AMV (NVI-CTRL and NVI-NIN-AMV) do, which suggests the assimilation of enhanced AMVs in the TC inner-core region can strengthen the performance of TC intensity forecast in HWRf for these two cases.

Despite the positive impacts of enhanced AMVs on hurricane forecasts in the above analyses, the impact of enhanced AMVs on HWRf forecasts may not be substantial in most cases like Joaquin. This is not only because of the availability of rapid scan imagery and the different

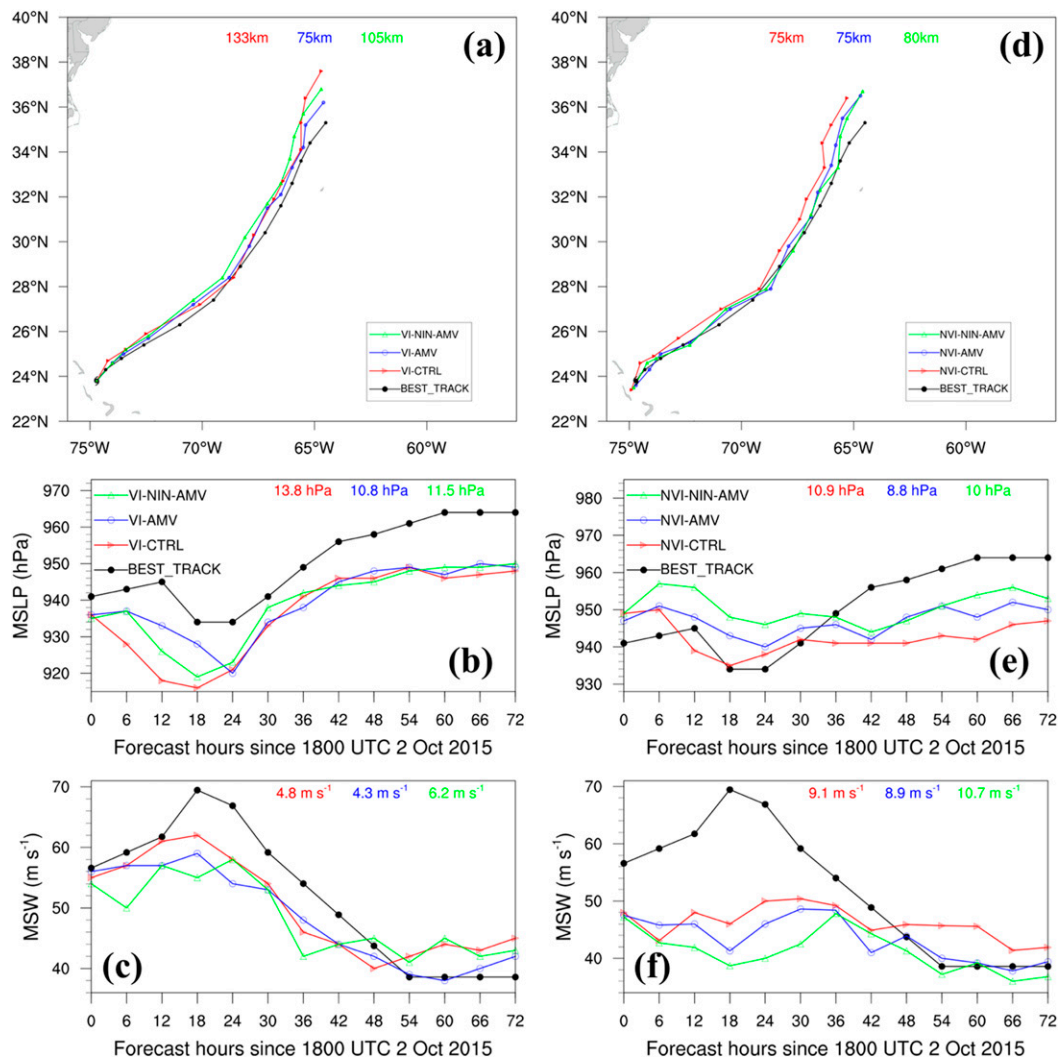


FIG. 8. The 72-h HWRf forecast from (a)–(c) DA with VI and (d)–(f) DA without VI experiments for Hurricane Joaquin during the period from 1800 UTC 2 Oct to 1800 UTC 5 Oct 2015.

data coverage for different cases, but also because a lot of observations from other resources have already been assimilated in the HWRf DA system. Nevertheless, the enhanced AMVs data still show significant positive impacts on the certain period of forecasts of Hurricane Gonzalo. This should be especially true when the operational data are sparse within the hurricane inner-core region, while the enhanced AMVs supply good coverage of data.

4. Impacts of enhanced AMVs on hurricane initialization and forecast

a. Fit to observations

To obtain further insights into the influence of the enhanced AMVs on the initial analyses, especially in the hurricane inner-core region, $o - a$ (differences between

AMV observations and analyses) and $o - b$ (differences between AMV observations and background fields) are investigated for experiments VI-AMV and NVI-AMV over the innermost domain (d03 in Fig. 1) for Hurricane Gonzalo during the 24-h data assimilation period from 0000 to 1800 UTC 13 October 2014. Although direct comparisons of VI-AMV and NVI-AMV may be misleading because of configuration differences, as noted earlier, it is still informative to examine the relative impacts of the enhanced AMVs in these two scenarios. Figure 10 illustrates a histogram of wind speed departure from observations. It is obvious that the assimilation of enhanced AMVs leads to improvements in the fit of initial conditions to observations. Specifically, for NVI-AMV, the $o - a$ (Fig. 10a), with a range of $[-7.1, 5.7] \text{ m s}^{-1}$, is reduced significantly from $o - b$, with a range of $[-12.2, 9.5] \text{ m s}^{-1}$. For VI-AMV, the $o - a$

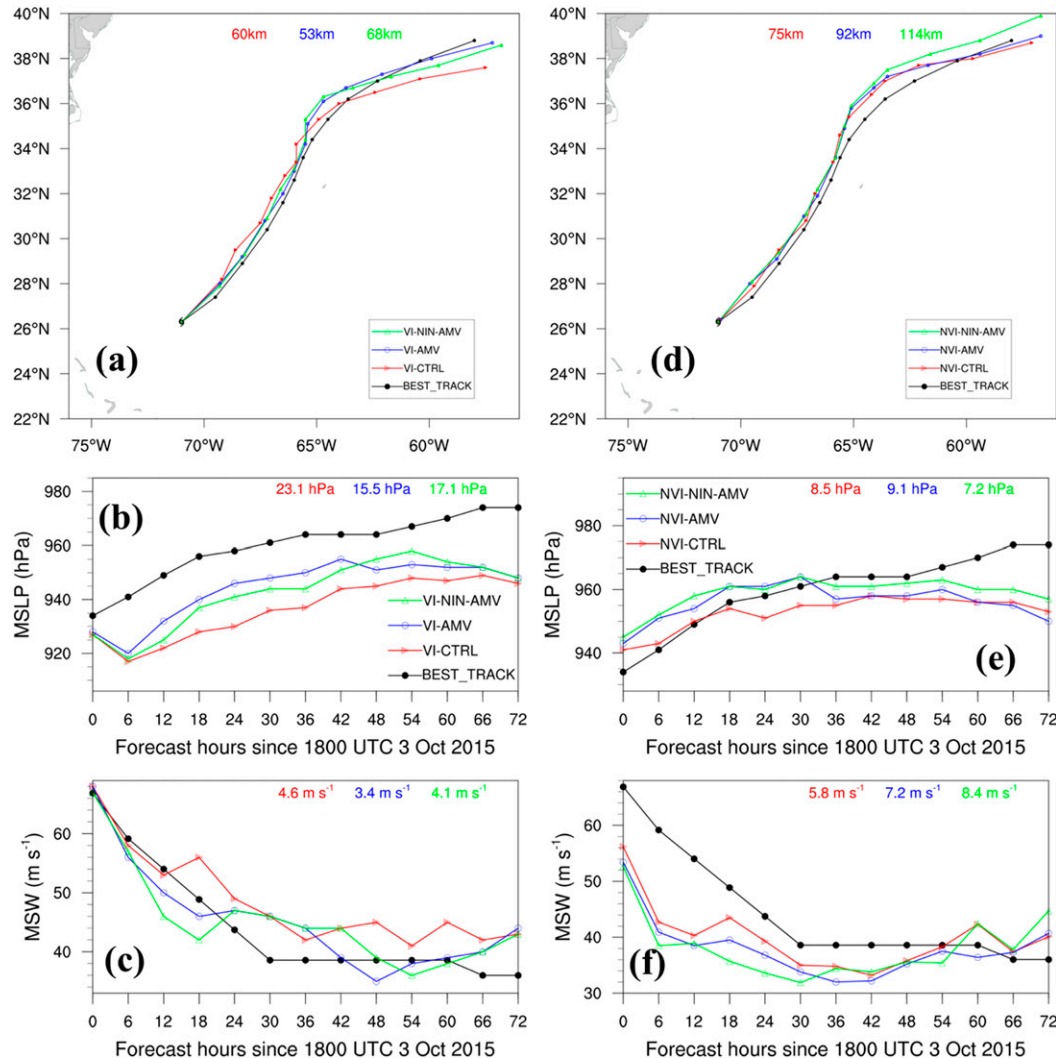


FIG. 9. As in Fig. 8, but for the 72-h HWRP forecast for Hurricane Joaquin during the period from 1800 UTC 3 Oct to 1800 UTC 6 Oct 2015.

(Fig. 10b) for wind speed, with a range of $[-7.5, 7.1] \text{ m s}^{-1}$, is substantially reduced, compared with the $o - b$, with a range of $[-8.3, 12.6] \text{ m s}^{-1}$. There are about 793 (1302) observations in which the differences fall within $\pm 0.25 \text{ m s}^{-1}$ in $o - b$ ($o - a$). Similar features are also observed in the fit of analysis wind direction to observations (figures not shown), suggesting that the assimilation of enhanced AMVs can improve both wind speed and wind direction analyses in the HWRP.

In addition, a total of 3545 (1513) enhanced AMVs are rejected by the DA system in VI-AMV (NVI-AMV) for Hurricane Gonzalo, leading to a total of 6580 (8612) enhanced AMVs with data assimilated within the d03 region for VI-AMV (NVI-AMV) at 0000, 0600, 1200, and 1800 UTC 24 October 2014. Despite the other configuration differences between VI-AMV and NVI-AMV, the

results here indicate that the VI in VI-AMV is also an important factor in increasing the data rejection rate in the DA system and reducing the number of enhanced AMVs assimilated into the DA system. As will be discussed in the next section, since VI in VI-AMV fails to provide realistic HWRP background fields in some cases, large $o - b$ values could occur in these cases and lead to more data rejection during the gross checking procedure embedded in the GSI. However, the $o - a$ differences in VI-AMV have nearly the same distribution as those in NVI-AMV, implying that the improvements in the fit of initial conditions to observations can still be achieved in VI-AMV, although the DA system assimilates fewer enhanced AMVs. This can partially explain the positive impact of VI-AMV on hurricane forecasts, compared with VI-CTRL.

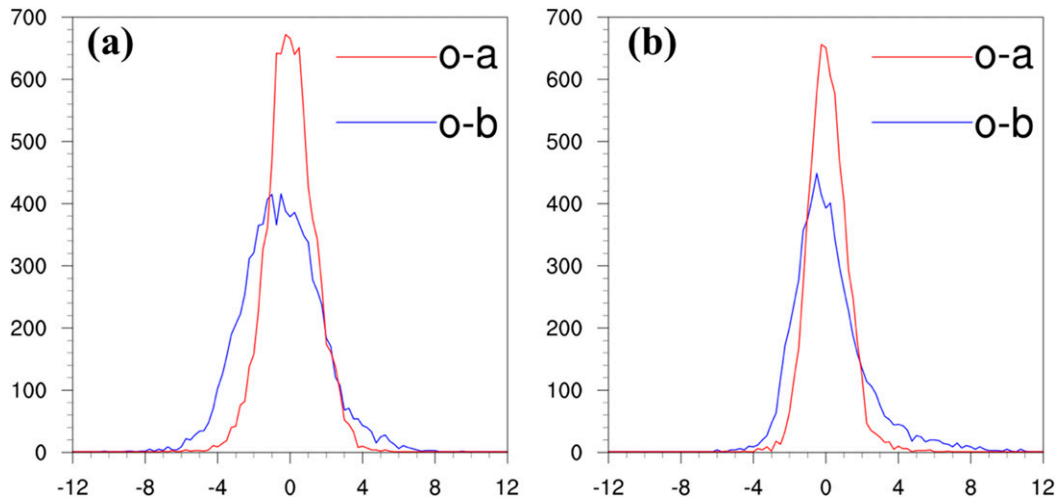


FIG. 10. Histogram of wind speed departure from observations for HWRf first-guess winds ($o - b$, blue lines) and HWRf analyzed winds ($o - a$, red lines) from (a) NVI-AMV and (b) VI-AMV experiments for Hurricane Gonzalo. The departure is calculated for the enhanced AMV data in the HWRf d03 domain from the first-guess and analysis fields at 0000, 0600, 1200, and 1800 UTC 3 Oct 2014. The horizontal axis denotes the wind speed departure (m s^{-1}), and the vertical axis denotes the number of observations.

b. Impacts on initial analysis

To quantitatively evaluate the impacts of assimilating enhanced AMVs on the initial conditions, following Wang (2014), the mean equitable threat scores (ETSs) are calculated for the 10-m wind analysis fields from VI-CTRL (NVI-CTRL) and VI-AMV (NVI-AMV), compared against the Aircraft-based Tropical Cyclone Surface Wind Analysis (ATCSWA) fields during the DA period for Hurricane Gonzalo from 0000 to 1800 UTC 13 October 2014. The ATCSWA data are provided by NOAA/National Environmental Satellite, Data, and Information Service (NESDIS) and depict the 10-m wind analysis field within a $10^\circ \times 10^\circ$ box around the storm center. Previous studies have shown that ATCSWA can well reproduce the basic vortex structure and realistic wind analysis field around the storm (Knaff and Zehr 2007; Knaff et al. 2015). As depicted in Fig. 11, the mean ETSs in VI-AMV are higher than those in VI-CTRL for all thresholds from 2 to 20 m s^{-1} (Fig. 11a), while the mean ETSs in NVI-AMV are higher than those in NVI-CTRL for the thresholds from 2 to 10 m s^{-1} (Fig. 11a). This result indicates that the experiments with the assimilation of enhanced AMVs produce more skillful wind analyses than those without the assimilation of enhanced AMVs. Since the ETSs measure the quantitative forecast accuracy relative to the observational or analysis field, these results also demonstrate that assimilation of enhanced AMVs improves the initial conditions for HWRf forecasts in both the VI and NVI experiments.

c. Improving the initial imbalances in Hurricane Gonzalo

As mentioned in section 3, an unrealistic vortex weakening appears in the experiments of VI-CTRL and VI-NIN-AMV for Hurricane Gonzalo, although it is not shown after 6-h forecasts in these experiments without VI (i.e., NVI-CTRL, NVI-NIN-AMV, and NVI-AMV) or in the VI with the assimilation of enhanced AMVs in the inner-core region (VI-AMV). These results suggest that the VI plays a role in the unrealistic vortex weakening, and the assimilation of enhanced AMVs in the inner-core region may help mitigate this problem.

To further support this, a diagnosis is conducted into the gradient wind balance, following Pu et al. (2016). Willoughby (1990) and Smith et al. (2009) commented that the azimuthal-mean tangential circulation in the TC inner-core region approximately follows the gradient wind balance relationship in pressure coordinates:

$$F = -g \frac{\partial z}{\partial r} + \frac{v^2}{r} + f_0 v, \quad (1)$$

where g is gravitational acceleration, z is geopotential height, v is the tangential wind speed, f_0 is the Coriolis parameter at the storm center, and F represents the net radial force field, which is defined as the difference between the local radial pressure gradient and the sum of the centrifugal and Coriolis forces by Smith et al. (2009). If $F = 0$, the tangential flow is in exact gradient wind balance; if $F < 0$, the flow is subgradient; and if $F > 0$, it is supergradient. Note that all variables in Eq. (1) are in azimuthal average framework.

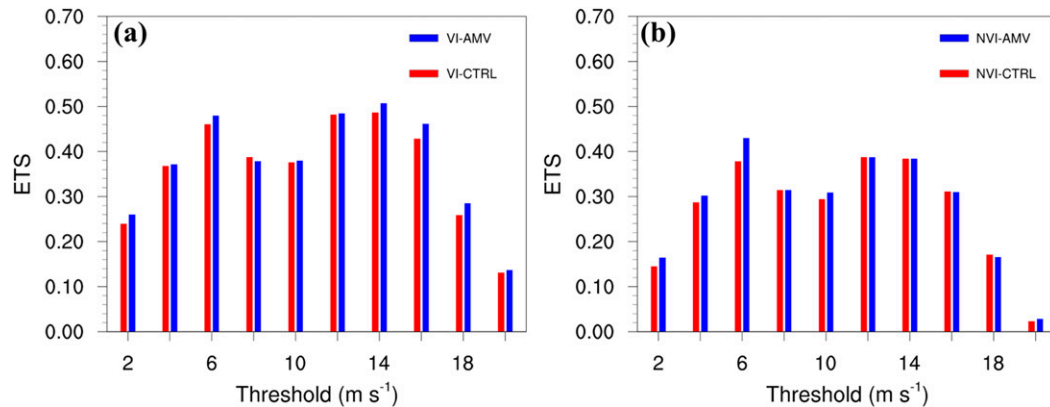


FIG. 11. Mean ETSs of the 10-m forecasted wind field from (a) VI-CTRL (red bars) and VI-AMV (blue bars) and (b) NVI-CTRL (red bars) and NVI-AMV (blue bars), compared against the 10-m wind analysis from ATCSWA with thresholds of 2, 4, 6, 8, 10, 12, 14, 16, 18, and 20 m s^{-1} . The mean ETS is calculated during the DA period of Hurricane Gonzalo from 0000 to 1800 UTC 13 Oct 2014 with a 6-h interval.

Figure 12 compares radius–height cross sections of F isopleths in the vortex from the HWRP background before VI and the vortex generated by HWRP VI (before DA, namely, the result of vortex relocation, size, and intensity correction) for Hurricane Gonzalo at 1800 UTC 13 October 2014. According to Smith et al. (2009), the subgradient due to friction in the boundary layer and the supergradient when air parcels are ejected upward and outward on top of the subgradient flow can be observed in the lower troposphere (e.g., below 850 hPa) over a region within 0–150-km radius to storm center ($r = 0$ –150 km). Consistently, these features are also clearly seen in VI-CTRL/VI-AMV after the vortex initialization (Figs. 12c,d). However, the vortex in the HWRP background before the VI from VI-CTRL/VI-AMV satisfies the gradient wind balance in its upper level within $r = 0$ –150-km region (Figs. 12a,b), while supergradient winds are present in the upper level within $r = 0$ –150-km region of the HWRP vortex in VI-CTRL/VI-AMV due to its VI procedure (Figs. 12c,d). In addition, a subgradient/supergradient wind is also clearly seen in the lower boundary layer (below 850 hPa) of the vortex after the vortex initialization (Figs. 12c,d). These features are not consistent with the results from previous studies (e.g., Smith et al. 2009).

Figure 13 compares radius–height cross sections of F isopleths in VI-CTRL and VI-AMV at HWRP analysis time (1800 UTC 13 October 2014) and its 12-h forecast (0600 UTC 14 October 2014; after the unrealistic vortex weakening). At the analysis time, the supergradient winds appear in the upper level within $r = 0$ –150-km region in VI-CTRL (Fig. 13a), while in VI-AMV, the gradient wind balance is more closely established, especially above 500 hPa (Fig. 13b). In addition, the

supergradient wind distribution in Fig. 13a is similar to that in Fig. 12c, indicating that the supergradient wind imbalances in the upper level within $r = 0$ –150-km region seem to be dominated by the VI in all experiments with VI. For the 12-h forecast shown in Fig. 13c, the gradient wind imbalances disappear in the $r = 0$ –150-km region above 500 hPa in VI-CTRL after the unrealistic vortex weakening. Meanwhile, there is no substantial adjustment in gradient wind structure in VI-AMV during this 12-h forecast (Fig. 13d). Therefore, the results here suggest that gradient wind imbalance produced by VI exists in the HWRP initial vortex in VI-CTRL. These imbalances are possibly related to the artificial specification of the vortex structure in VI during its relocation, size, and intensity corrections. Data assimilation with enhanced AMVs in both the storm environment and inner-core regions can reduce this initial vortex imbalance to a great extent. This is possibly because the data from enhanced AMVs in the inner-core region could provide additional constraints to mitigate the dynamical and physical imbalances in the first guess (e.g., analysis with VI), resulting in a more balanced initial analysis for Hurricane Gonzalo.

Moreover, the imbalances for other experiments are also checked (figures not shown). It is found that the distribution of F in VI-NIN-AMV is similar to that in VI-CTRL, as the supergradient wind imbalances are shown in the upper troposphere in VI-CTRL. According to Table 2, the data assimilated in ghost d03 for VI-NIN-AMV and VI-CTRL are the same, implying that assimilation of the enhanced AMVs in the storm environment region only (ghost d02) will not reduce the imbalances within $r = 0$ –150-km region. Furthermore, the imbalances also exist in the NVI experiments after

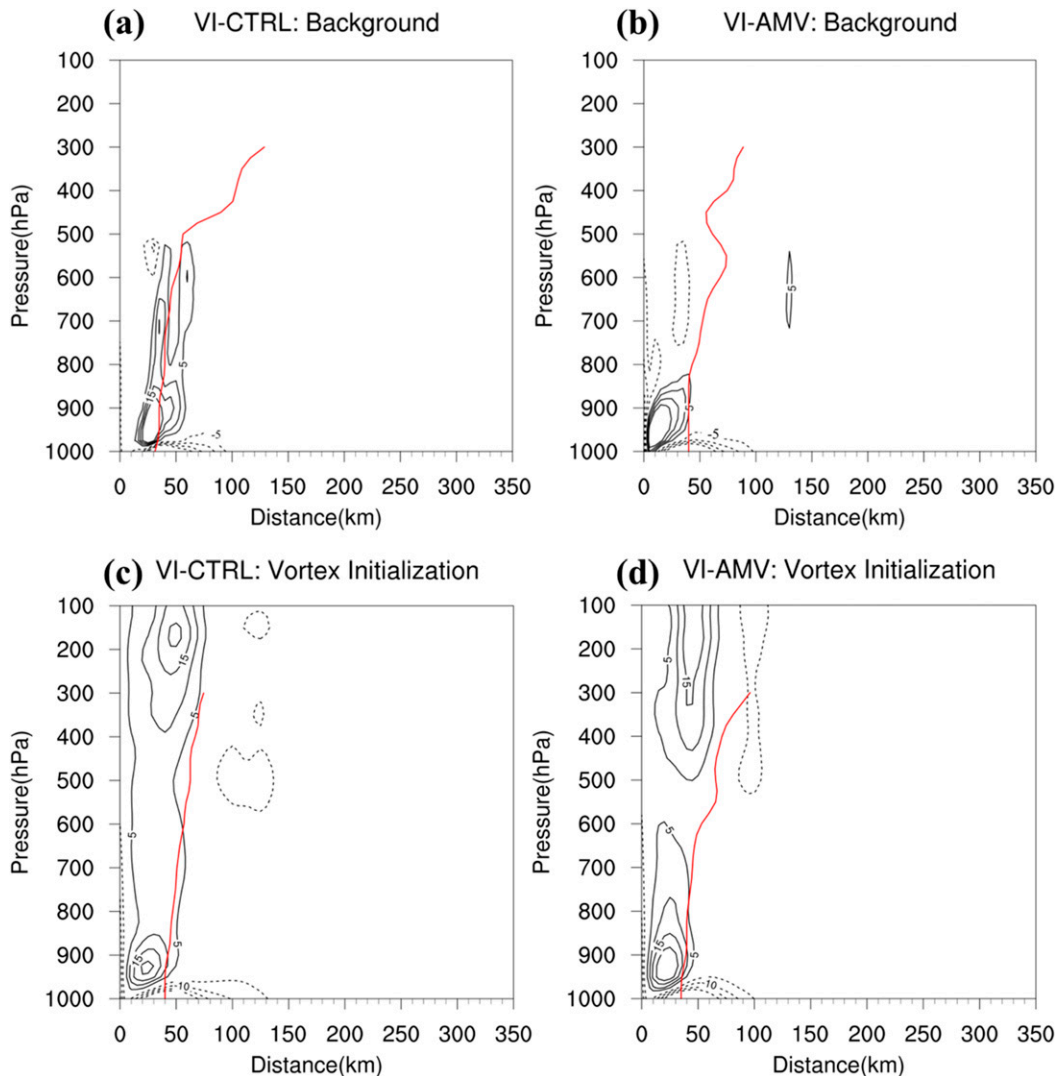


FIG. 12. Radius–height cross sections of the isopleths of the net radial force per unit mass from (a) HWRF background in VI-CTRL, (b) HWRF background in VI-AMV, (c) VI (before DA) in VI-CTRL, and (d) VI in VI-AMV for Hurricane Gonzalo at 1800 UTC 13 Oct 2014. The contour interval is $5 \text{ m s}^{-1} \text{ h}^{-1}$, with dashed lines indicating negative values. The zero contour is not plotted. The red lines indicate the radius of maximum wind. The figures for HWRF analyses are generated by using the data in d03.

DA at 1800 UTC 13 October 2014, but the magnitude of F is weaker than that in VI-CTRL (figures not shown), implying that the gradient wind imbalances can also exist in the initial analysis even without VI. The imbalances are possibly from the data assimilation as the model adjusts to the analysis increments. However, the large magnitude of F in VI-CTRL suggests that the additional gradient wind imbalances are imposed by VI, leading to the unrealistic gradient wind imbalances in the initial vortex (e.g., upper level within $r = 0\text{--}150\text{-km}$ region) and imbalances in VI-CTRL for Hurricane Gonzalo. Thus, the improvements in the initial vortex balance in VI-AMV are due to the

assimilation of enhanced AMVs. Nevertheless, an open question here is how to quantify the threshold of imbalances (e.g., gradient wind imbalance) that the HWRF Model can accept or handle, which is beyond the scope of this study; thus, it should be pursued in future studies.

d. Improving the unrealistic vortex weakening of Hurricane Gonzalo

We further examine the unrealistic weakening of Hurricane Gonzalo. Figure 14 illustrates the azimuthally averaged radial velocity (shading) from the GFS analysis, VI-CTRL, and VI-AMV initial conditions at

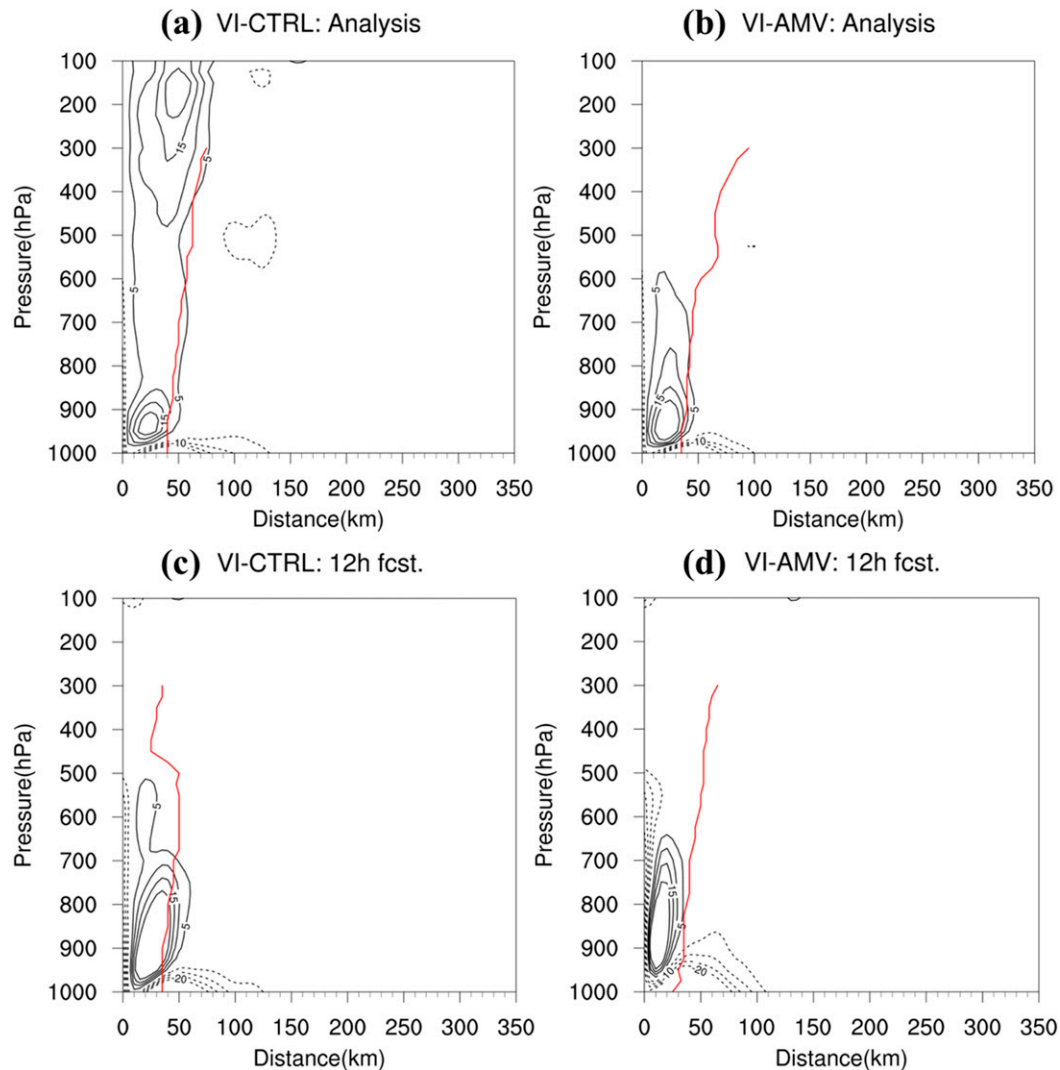


FIG. 13. As in Fig. 12, but for the analysis field from (a),(c) VI-CTRL and (b),(d) VI-AMV for Hurricane Gonzalo at (a),(b) 1800 UTC 13 Oct and (c),(d) 12-h forecasts at 0600 UTC 14 Oct 2014.

1800 UTC 13 October 2014. Since the GFS analysis is at a coarser resolution, compared with the HWRF high-resolution analysis, we use these comparisons only to verify the general features of the hurricane secondary circulation. It is confirmed that the VI-AMV analysis (Fig. 14c) leads to a secondary circulation of Hurricane Gonzalo that is close to the main features in the GFS analysis (Fig. 14a). Meanwhile, VI-CTRL (Fig. 14b) leads to weaker upper-layer outflow (above 300 hPa) over the region within 0–350-km radius to storm center ($r = 0$ –350 km) than the GFS analysis (Fig. 14a) and VI-AMV do (Fig. 14c). A strong outflow between 500 and 300 hPa within $r = 0$ –350-km region is also shown in VI-CTRL (Fig. 14b), while these features are not shown in the GFS (Fig. 14a) analysis and VI-AMV (Fig. 14c).

In addition, the secondary circulation is asymmetric in VI-CTRL, as the strong low-level inflow is concentrated within 0–200 km of radius and the strong upper-level outflow is concentrated within 150–350 km of radius, while this is not obvious in the GFS analysis (Fig. 14a) and VI-AMV (Fig. 14c).

Figure 14d compares the total displacement of the vortex centers at various pressure levels from the center at 1000 hPa among GFS analysis, VI-CTRL, and VI-AMV. Following Frank and Ritchie (2001), the vortex positions are estimated from the minimum geopotential height at each pressure level, and no tilt is calculated when the geopotential height minimum is no longer distinct (above 250 hPa). Note that the horizontal grid spacing is ~ 25 km in the GFS analysis

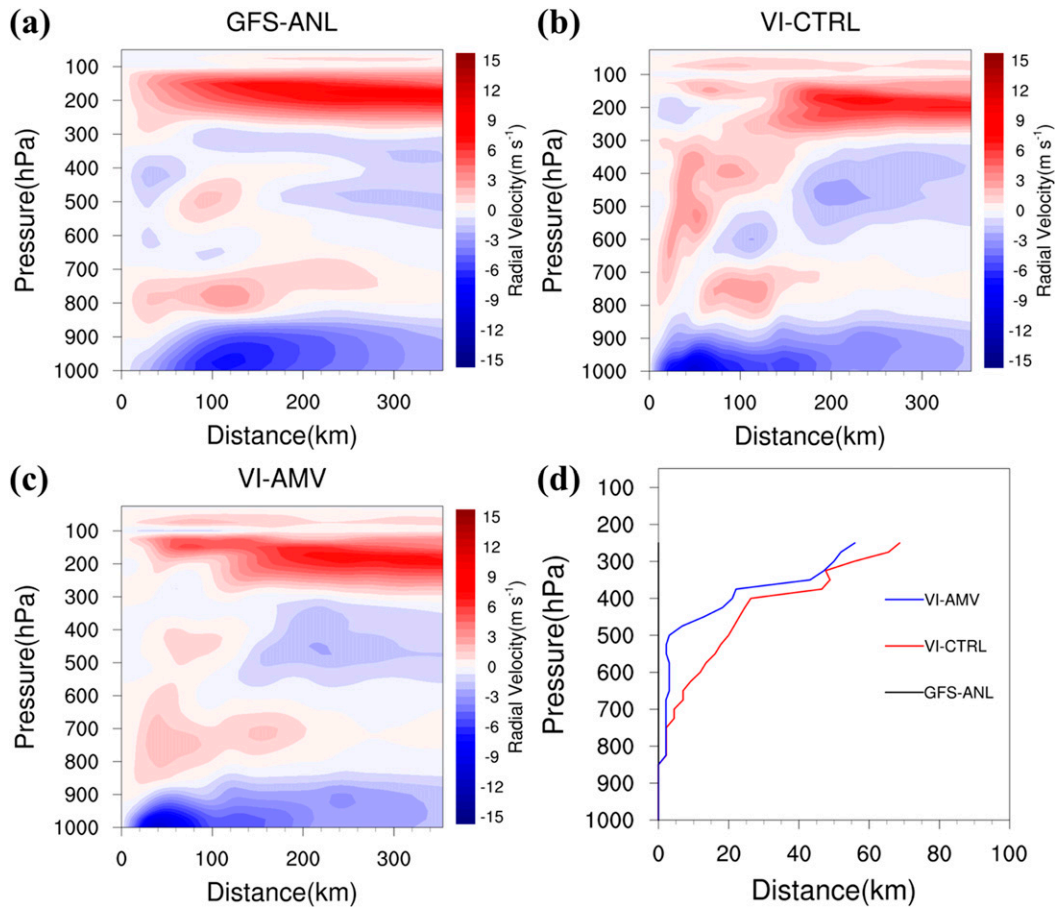


FIG. 14. The azimuthally averaged radial wind (color contours; m s^{-1}) from (a) GFS analysis, (b) VI-CTRL, and (c) VI-AMV for Hurricane Gonzalo at 1800 UTC 13 Oct 2014. (d) Total displacement (km) of the storm center at each pressure level from the storm center at 1000 hPa for (a)–(c). The figures for HWRF forecasts are generated by using the data in d03.

and ~ 2 km in VI-CTRL and VI-AMV. Tilts of ~ 25 km or less in the GFS analysis and of ~ 2 km or less in VI-CTRL and VI-AMV are not resolved. As shown in Fig. 14d, the storm does not tilt from 1000 to 250 hPa in the GFS analysis (black line), but begins to tilt at about 500 hPa in VI-AMV and at about 850 hPa in VI-CTRL. In addition, the magnitude of tilt at 500 hPa is ~ 30 km in VI-CTRL, while it is ~ 5 km in VI-AMV and 0 km in the GFS analysis. The vertical tilting in VI-CTRL is much stronger than that in VI-AMV and the GFS analysis. The tilt of the eye can be hostile to the storm intensification due to ventilation. VI-CTRL leads to larger tilt than VI-AMV does, indicating that the atmospheric conditions in VI-CTRL are less favorable for the intensification of Hurricane Gonzalo than those in VI-AMV are.

Figure 15 shows the azimuthally averaged relative humidity (green contours), temperature perturbation (shading), and secondary circulation (vectors) from

VI-CTRL and VI-AMV for Hurricane Gonzalo from the 6-h forecast valid at 0000 UTC 14 October 2014. The azimuthally averaged temperature perturbations are calculated as differences between the temperatures near the simulated circulation center (0–350 km of radius) and the environmental temperature, which is determined by averaging the temperature within the whole area of the nested domain 3. It is seen that VI-CTRL (Fig. 15a) leads to a weaker secondary circulation, upper-level warming, and lower midlevel relative humidity than VI-AMV (Fig. 13b). Specifically, the upper-level outflow (above 300 hPa) in VI-CTRL is $1\text{--}5 \text{ m s}^{-1}$ smaller than in VI-AMV (Fig. 15c). The maximum temperature difference between VI-AMV and VI-CTRL in the upper level within the hurricane inner core is above 2°C , and the midlevel relative humidity in VI-CTRL is 5%–50% smaller than that in VI-AMV (Fig. 15c). Higher midlevel moisture and upper-level warming in

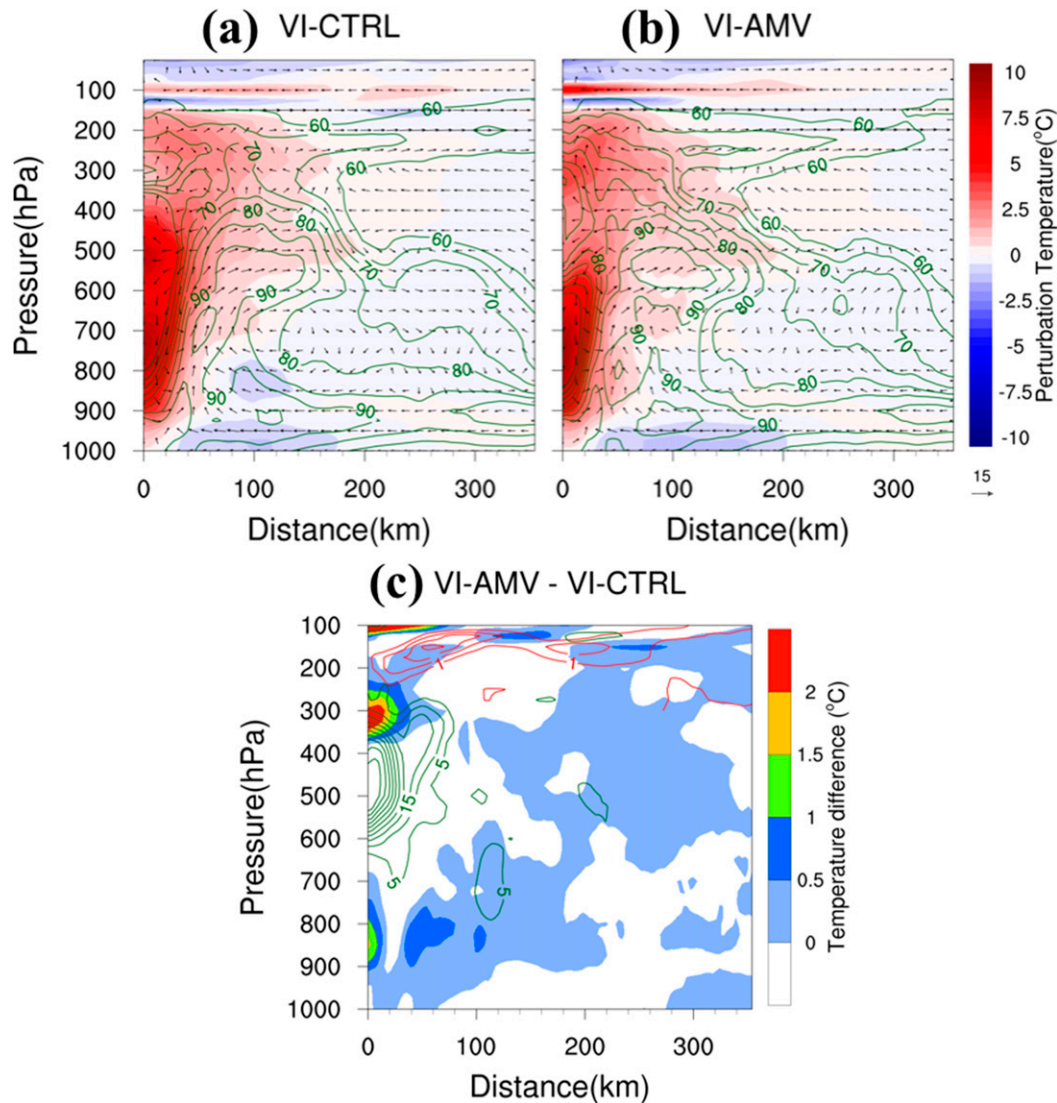


FIG. 15. The azimuthally averaged relative humidity (green contours in 5% intervals; only contours above 60% are shown), temperature perturbation (shading), secondary circulation [represented by $\mathbf{u-w}$ vectors; \mathbf{u} (radial velocity), m s^{-1} ; \mathbf{w} (vertical velocity), cm s^{-1}] in 6-h HWRF forecast from (a) VI-CTRL and (b) VI-AMV for Hurricane Gonzalo valid at 0000 UTC 14 Oct 2014. (c) The differences of azimuthally averaged temperature (shading; only positive values are shown), relative humidity (green contours in 5% intervals), and radial velocity above 300 hPa (red contours in 2 m s^{-1} intervals) between VI-AMV and VI-CTRL. The azimuthally averaged values are calculated as differences between the temperatures near the simulated circulation center (0–300 km) and the environmental temperature, which is determined by averaging the temperature within the whole of domain 3.

the region around the storm center (e.g., $r = 0\text{--}350 \text{ km}$) have been shown to be essential for rapid intensification (RI) (Malkus and Riehl 1960; Holland 1997; Zhang and Chen 2012; Chen and Zhang 2013). Thus, VI-CTRL presents less favorable conditions for RI of Hurricane Gonzalo, compared with VI-AMV. These results help explain why VI-CTRL does not capture the RI of Hurricane Gonzalo.

Overall, the unrealistic vortex weakening problem in VI-CTRL for Hurricane Gonzalo is associated with unrealistic upper-level outflow structure and more unfavorable thermodynamic conditions during the RI of Hurricane Gonzalo. It leads to the degradation of HWRF intensity forecasts in VI-CTRL. The assimilation of enhanced AMVs in the inner-core region improves the unrealistic outflow structure and unfavorable

thermodynamical conditions to some extent. As a result, the unrealistic vortex weakening is mostly mitigated, and the intensity forecasts are improved in VI-AMV.

5. Summary and discussion

In this study, DA experiments and numerical simulations are conducted using the HWRf Model and its GSI-based ensemble-variational hybrid DA system to predict the intensification phase of Hurricanes Gonzalo (2014) and three intensity change periods of Joaquin (2015). Different to previous studies, we enable the DA of enhanced AMV dataset (produced from GOES satellites in a demonstration mode by CIMSS at the University of Wisconsin) in the HWRf innermost model domain (i.e., the TC inner-core region), and the impacts of inner-core DA from enhanced AMV datasets on the intensity prediction of the two hurricanes are evaluated. Two different DA strategies, one including HWRf operational settings that use a combination of VI with DA in each analysis cycle (“DA with VI”) and another using a pure DA with all available data (“DA without VI”), are utilized. Results from these experiments on HWRf initial analyses and forecasts are examined. It is found that in both the “DA with VI” and “DA without VI” experiments, the inner-core DA of enhanced AMVs leads to promising improvements in track and intensity forecasts, while assimilating the enhanced AMVs outside the inner domain leads to more limited impacts. This indicates that inner-core AMV information could be an important source for HWRf initialization.

For Hurricane Gonzalo, inner-core assimilation of enhanced AMVs alleviated much of the unrealistic vortex weakening problem induced by the HWRf VI, leading to significant positive impacts on track and intensity forecasts. For Hurricane Joaquin, the assimilation of enhanced AMVs leads to slight positive impacts on the track and intensity forecast during the three intensity change periods for both “DA with VI” and “DA without VI” experiments. The assimilation of enhanced AMVs in the inner-core region leads to the overall best results than other DA configurations.

It is further found that VI has potential negative impacts on the DA of enhanced AMVs in Hurricane Gonzalo, as the VI before DA alters the first guess, thus influencing the DA through quality control process, and reduces the actual number of AMV observations assimilated into the DA system. Also, it is shown that the VI before DA can impose unrealistic gradient wind imbalances on Hurricane Gonzalo, and the assimilation of enhanced AMVs in the inner-core region can mitigate these imbalances, thus offering better initial conditions

for the intensity forecast of Hurricane Gonzalo. Moreover, diagnoses on the dynamical and thermodynamical fields suggest that the unrealistic vortex weakening in VI experiments for Hurricane Gonzalo is associated with unrealistic upper-level outflow structure and unfavorable thermodynamic conditions for the rapid intensification of Hurricane Gonzalo, leading to the degradation of intensity forecasts. Meanwhile, assimilation of enhanced AMVs in the inner-core region can help improve the unrealistic outflow structure and unfavorable thermodynamic conditions. As a result, the intensity forecasts are improved.

Despite the positive impacts of enhanced AMVs on hurricane forecast, it should be pointed out that the impact of enhanced AMVs on HWRf forecast may not be substantial in most of the cases like Joaquin. On the one hand, the availability of rapid scan imagery and derivation approach used for AMV retrieval can lead to different data coverages for different cases. Limited data impact is expected if the data coverage around the storm is sparse. On the other hand, many observations from other resources (e.g., dropsonde and radar) have already been assimilated in the HWRf DA system, leaving little room for the data impact from enhanced AMVs. Thus, the positive impact of enhanced AMV data on HWRf forecasts could only be found in a certain forecast period or for a specific hurricane, such as Gonzalo. This is especially true when the operational data are sparse around the storm center, while the enhanced AMVs enable good data coverage. As discussed for the Gonzalo case, with the data from enhanced AMVs, the DA could also improve the model initial conditions and mitigate the adverse effect of VI, resulting in improvements in the hurricane forecasts.

Results from this study are encouraging but encompass only two hurricane cases. A larger sample of TC cases will be necessary in order to evaluate the consistency of the forecast impact on the HWRf Model provided by enhanced AMV data. In addition, results from this study further prove that the configuration of data assimilation can play an essential role in data impacts, leading to forecast improvements. Future work should emphasize data assimilation methods that enhance the impacts from various observations (i.e., AMVs).

Acknowledgments. This study is supported by NOAA/NWS Awards NA14NWS4680025 (Pu and Zhang) and NA10NES4400013 (Velden), Office of Naval Research Awards N000141310582 (Pu) and N00014-14-1-0116 (Velden), and NASA Award NNX13AQ38G (Pu and Zhang). The NOAA Jet supercomputer, supported by NOAA/ESRL and the Center for High-Performance

Computing (CHPC) at the University of Utah, is greatly appreciated. Dave Stettner of CIMSS is acknowledged for processing and providing the enhanced AMV datasets for Hurricanes Gonzalo and Joaquin. Review comments from three anonymous reviewers and Dr. Tyan Torn (editor) were very helpful for improving the manuscript.

REFERENCES

- Aligo, E., B. Ferrier, J. Carley, E. Rodgers, M. Pyle, S. J. Weiss, and I. L. Jirak, 2014: Modified microphysics for use in high-resolution NAM forecasts. *27th Conf. on Severe Local Storms*, Madison, WI, Amer. Meteor. Soc., 16A.1, <https://ams.confex.com/ams/27SLS/webprogram/Paper255732.html>.
- Bao, J.-W., S. G. Gopalakrishnan, S. A. Michelson, F. D. Marks, and M. T. Montgomery, 2012: Impact of physics representations in the HWRF on simulated hurricane structure and pressure–wind relationships. *Mon. Wea. Rev.*, **140**, 3278–3299, <https://doi.org/10.1175/MWR-D-11-00332.1>.
- Berg, R., 2016: Tropical cyclone report: Hurricane Joaquin, 28 September–7 October 2015. NOAA/NHC Tech. Rep. AL112015, 36 pp., http://www.nhc.noaa.gov/data/tcr/AL112015_Joaquin.pdf.
- Berger, H., R. Langland, C. S. Velden, C. A. Reynolds, and P. M. Pauley, 2011: Impact of enhanced satellite-derived atmospheric motion vector observations on numerical tropical cyclone track forecasts in the western North Pacific during TPARC/TCS-08. *J. Appl. Meteor. Climatol.*, **50**, 2309–2318, <https://doi.org/10.1175/JAMC-D-11-019.1>.
- Black, P. G., and Coauthors, 2007: Air–sea exchange in hurricanes: Synthesis of observations from the coupled boundary layer air–sea transfer experiment. *Bull. Amer. Meteor. Soc.*, **88**, 357–374, <https://doi.org/10.1175/BAMS-88-3-357>.
- Brown, D. P., 2014: Tropical cyclone report: Hurricane Gonzalo, 12–19 October 2014. NOAA/NHC Tech. Rep. AL082014, 30 pp., http://www.nhc.noaa.gov/data/tcr/AL082014_Gonzalo.pdf.
- Chen, F., and J. Dudhia, 2001: Coupling an advanced land surface–hydrology model with the Penn State–NCAR MM5 modeling system. Part I: Model implementation and sensitivity. *Mon. Wea. Rev.*, **129**, 569–585, [https://doi.org/10.1175/1520-0493\(2001\)129<0569:CAALSH>2.0.CO;2](https://doi.org/10.1175/1520-0493(2001)129<0569:CAALSH>2.0.CO;2).
- Chen, H., and D.-L. Zhang, 2013: On the rapid intensification of Hurricane Wilma (2005). Part II: Convective bursts and the upper-level warm core. *J. Atmos. Sci.*, **70**, 146–162, <https://doi.org/10.1175/JAS-D-12-062.1>.
- Ferrier, B. S., 2005: An efficient mixed-phase cloud and precipitation scheme for use in operational NWP models. *Eos, Trans. Amer. Geophys. Union*, **86** (Spring Meeting Suppl.), Abstract A42A-02.
- , Y. Jin, Y. Lin, T. Black, E. Rogers, and G. DiMego, 2002: Implementation of a new grid-scale cloud and precipitation scheme in the NCEP Eta model. *19th Conf. on Weather Analysis and Forecasting/15th Conf. on Numerical Weather Prediction*, San Antonio, TX, Amer. Meteor. Soc., 10.1, https://ams.confex.com/ams/SLS_WAF_NWP/techprogram/paper_47241.htm.
- Frank, W. M., and E. A. Ritchie, 2001: Effects of vertical wind shear on the intensity and structure of numerically simulated hurricanes. *Mon. Wea. Rev.*, **129**, 2249–2269, [https://doi.org/10.1175/1520-0493\(2001\)129<2249:EOVWSO>2.0.CO;2](https://doi.org/10.1175/1520-0493(2001)129<2249:EOVWSO>2.0.CO;2).
- Gall, R., J. Franklin, F. Marks, E. N. Rappaport, and F. Toepfer, 2013: The Hurricane Forecast Improvement Project. *Bull. Amer. Meteor. Soc.*, **94**, 329–343, <https://doi.org/10.1175/BAMS-D-12-00071.1>.
- Gopalakrishnan, S. G., F. Marks, X. Zhang, J.-W. Bao, K.-S. Yeh, and R. Atlas, 2011: The experimental HWRF system: A study on the influence of horizontal resolution on the structure and intensity changes in tropical cyclones using an idealized framework. *Mon. Wea. Rev.*, **139**, 1762–1784, <https://doi.org/10.1175/2010MWR3535.1>.
- Han, J., and H.-L. Pan, 2011: Revision of convection and vertical diffusion schemes in the NCEP Global Forecast System. *Wea. Forecasting*, **26**, 520–533, <https://doi.org/10.1175/WAF-D-10-05038.1>.
- Holland, G. J., 1997: The maximum potential intensity of tropical cyclones. *J. Atmos. Sci.*, **54**, 2519–2541, [https://doi.org/10.1175/1520-0469\(1997\)054<2519:TMPIOT>2.0.CO;2](https://doi.org/10.1175/1520-0469(1997)054<2519:TMPIOT>2.0.CO;2).
- Hong, S.-Y., and H.-L. Pan, 1996: Nonlocal boundary layer vertical diffusion in a medium-range forecast model. *Mon. Wea. Rev.*, **124**, 2322–2339, [https://doi.org/10.1175/1520-0493\(1996\)124<2322:NBLVDI>2.0.CO;2](https://doi.org/10.1175/1520-0493(1996)124<2322:NBLVDI>2.0.CO;2).
- Iacono, M. J., J. S. Delamere, E. J. Mlawer, M. W. Shephard, S. A. Clough, and W. D. Collins, 2008: Radiative forcing by long-lived greenhouse gases: Calculations with the AER radiative transfer models. *J. Geophys. Res.*, **113**, D13103, <https://doi.org/10.1029/2008JD009944>.
- Janjić, Z. I., R. Gall, and M. E. Pyle, 2010: Scientific documentation for the NMM Solver. NCAR Tech. Note NCAR/TN-477+STR, 53 pp.
- Kleist, D. T., D. F. Parrish, J. C. Derber, R. Treadon, W.-S. Wu, and S. Lord, 2009: Introduction of the GSI into the NCEP Global Data Assimilation System. *Wea. Forecasting*, **24**, 1691–1705, <https://doi.org/10.1175/2009WAF2222201.1>.
- Knaff, J. A., and R. M. Zehr, 2007: Reexamination of tropical cyclone wind–pressure relationships. *Wea. Forecasting*, **22**, 71–88, <https://doi.org/10.1175/WAF965.1>.
- , S. P. Longmore, R. T. DeMaria, and D. A. Molenaar, 2015: Improved tropical-cyclone flight-level wind estimates using routine infrared satellite reconnaissance. *J. Appl. Meteor. Climatol.*, **54**, 463–478, <https://doi.org/10.1175/JAMC-D-14-0112.1>.
- Kwon, Y. C., S. Lord, B. Lapenta, V. Tallapragada, Q. Liu, and Z. Zhang, 2010: Sensitivity of air–sea exchange coefficients (Cd and Ch) on hurricane intensity. *29th Conf. on Hurricanes and Tropical Meteorology*, Tucson, AZ, Amer. Meteor. Soc., 13C.1, https://ams.confex.com/ams/29Hurricanes/techprogram/paper_167760.htm.
- Langland, R. H., C. Velden, P. M. Pauley, and H. Berger, 2009: Impact of satellite-derived rapid-scan wind observations on numerical model forecasts of Hurricane Katrina. *Mon. Wea. Rev.*, **137**, 1615–1622, <https://doi.org/10.1175/2008MWR2627.1>.
- Liu, Q., N. Surgi, S. Lord, W.-S. Wu, S. Parrish, S. Gopalakrishnan, J. Waldrop, and J. Gamache, 2006: Hurricane initialization in HWRF model. *27th Conf. on Hurricanes and Tropical Meteorology*, Monterey, CA, Amer. Meteor. Soc., 8A.2, https://ams.confex.com/ams/27Hurricanes/techprogram/paper_108496.htm.
- Malkus, J. S., and H. Riehl, 1960: On the dynamics and energy transformations in steady-state hurricanes. *Tellus*, **12**(1), 1–20, <https://doi.org/10.3402/tellusa.v12i1.9351>.
- Mitchell, K., and Coauthors, 2005: The community Noah land surface model (LSM) user’s guide version 2.7.1. NOAA/NCEP Doc., 26 pp.
- Parrish, D., and J. Derber, 1992: The National Meteorological Center’s spectral statistical-interpolation analysis system. *Mon. Wea. Rev.*, **120**, 1747–1763, [https://doi.org/10.1175/1520-0493\(1992\)120<1747:TNMCSS>2.0.CO;2](https://doi.org/10.1175/1520-0493(1992)120<1747:TNMCSS>2.0.CO;2).

- Powell, M. D., P. J. Vickery, and T. A. Reinhold, 2003: Reduced drag coefficient for high wind speeds in tropical cyclones. *Nature*, **422**, 279–283, <https://doi.org/10.1175/2007WAF2007006.110.1038/nature01481>.
- Pu, Z., and S. Braun, 2001: Evaluation of bogus vortex techniques with four-dimensional variational data assimilation. *Mon. Wea. Rev.*, **129**, 2023–2039, [https://doi.org/10.1175/1520-0493\(2001\)129<2023:EOBVTW>2.0.CO;2](https://doi.org/10.1175/1520-0493(2001)129<2023:EOBVTW>2.0.CO;2).
- , X. Li, C. Velden, S. Abernson, and W. T. Liu, 2008: The impact of aircraft dropsonde and satellite wind data on numerical simulations of two landfalling tropical storms during the Tropical Cloud Systems and Processes Experiment. *Wea. Forecasting*, **23**, 62–79, <https://doi.org/10.1175/2007WAF2007006.1>.
- , —, and E. J. Zipser, 2009: Diagnosis of the initial and forecast errors in the numerical simulation of the rapid intensification of Hurricane Emily (2005). *Wea. Forecasting*, **24**, 1236–1251, <https://doi.org/10.1175/2009WAF2222195.1>.
- , S. Zhang, M. Tong, and V. Tallapragada, 2016: Influence of the self-consistent regional ensemble background error covariance on hurricane inner-core data assimilation with the GSI-based hybrid system for HWRF. *J. Atmos. Sci.*, **73**, 4911–4925, <https://doi.org/10.1175/JAS-D-16-0017.1>.
- Rappaport, E. N., and Coauthors, 2009: Advances and challenges at the National Hurricane Center. *Wea. Forecasting*, **24**, 395–419, <https://doi.org/10.1175/2008WAF2222128.1>.
- Rogers, R., and Coauthors, 2006: The Intensity Forecasting Experiment: A NOAA multiyear field program for improving tropical cyclone intensity forecasts. *Bull. Amer. Meteor. Soc.*, **87**, 1523–1538, <https://doi.org/10.1175/BAMS-87-11-1523>.
- , and Coauthors, 2013: NOAA's Hurricane Intensity Forecasting Experiment: A progress report. *Bull. Amer. Meteor. Soc.*, **94**, 859–882, <https://doi.org/10.1175/BAMS-D-12-00089.1>.
- Sears, J., and C. Velden, 2012: Validation of satellite-derived atmospheric motion vectors and analyses around tropical disturbances. *J. Appl. Meteor. Climatol.*, **51**, 1823–1834, <https://doi.org/10.1175/JAMC-D-12-024.1>.
- Smith, R. K., M. T. Montgomery, and N. Van Sang, 2009: Tropical cyclone spin-up revisited. *Quart. J. Roy. Meteor. Soc.*, **135**, 1321–1335, <https://doi.org/10.1002/qj.428>.
- Soden, B. J., C. S. Velden, and R. E. Tuleya, 2001: The impact of satellite winds on experimental GFDL hurricane model forecasts. *Mon. Wea. Rev.*, **129**, 835–852, [https://doi.org/10.1175/1520-0493\(2001\)129<0835:TIOSWO>2.0.CO;2](https://doi.org/10.1175/1520-0493(2001)129<0835:TIOSWO>2.0.CO;2).
- Tallapragada, V., and Coauthors, 2015: Hurricane Weather Research and Forecasting (HWRF) Model: 2015 scientific documentation. NCAR Tech. Note NCAR/TN-522+STR, 122 pp., <http://nldr.library.ucar.edu/collections/technotes/TECHNOTE-000-000-000-893.pdf>.
- Tong, M., V. Tallapragada, E. Liu, W. Wang, C. Kieu, Q. Liu, and B. Zhang, 2014: Impact of assimilating aircraft reconnaissance observations in operational HWRF. 2014 HFIP Annual Meeting, Miami, FL, HFIP, 21 pp., http://www.hfip.org/events/annual_meeting_nov_2014/wed/15_Tong_2014_HFIP_annual_meeting.pdf.
- Velden, C., and Coauthors, 2005: Recent innovations in deriving tropospheric winds from meteorological satellites. *Bull. Amer. Meteor. Soc.*, **86**, 205–224, <https://doi.org/10.1175/BAMS-86-2-205>.
- , C. M. Hayden, S. J. Nieman, W. P. Menzel, S. Wanzong, and J. S. Goerss, 1997: Upper-tropospheric winds derived from geostationary satellite water vapor observations. *Bull. Amer. Meteor. Soc.*, **78**, 173–196, [https://doi.org/10.1175/1520-0477\(1997\)078<0173:UTWDFG>2.0.CO;2](https://doi.org/10.1175/1520-0477(1997)078<0173:UTWDFG>2.0.CO;2).
- , W. Lewis, W. Bresky, D. Stettner, J. Daniels, and S. Wanzong, 2017: Assimilation of high-resolution satellite-derived atmospheric motion vectors: Impact on HWRF forecasts of tropical cyclone track and intensity. *Mon. Wea. Rev.*, **145**, 1107–1125, <https://doi.org/10.1175/MWR-D-16-0229.1>.
- Wang, C.-C., 2014: On the calculation and correction of equitable threat score for model quantitative precipitation forecasts for small verification areas: The example of Taiwan. *Wea. Forecasting*, **29**, 788–798, <https://doi.org/10.1175/WAF-D-13-00087.1>.
- Wang, X., D. Parrish, D. Kleist, and J. Whitaker, 2013: GSI 3DVar-based ensemble-variational hybrid data assimilation for NCEP Global Forecast System: Single-resolution experiments. *Mon. Wea. Rev.*, **141**, 4098–4117, <https://doi.org/10.1175/MWR-D-12-00141.1>.
- Willoughby, H. E., 1990: Gradient balance in tropical cyclones. *J. Atmos. Sci.*, **47**, 265–274, [https://doi.org/10.1175/1520-0469\(1990\)047<0265:GBITC>2.0.CO;2](https://doi.org/10.1175/1520-0469(1990)047<0265:GBITC>2.0.CO;2).
- Wu, W. S., R. J. Purser, and D. F. Parrish, 2002: Three-dimensional variational analysis with spatially inhomogeneous covariances. *Mon. Wea. Rev.*, **130**, 2905–2916, [https://doi.org/10.1175/1520-0493\(2002\)130<2905:TDVAWS>2.0.CO;2](https://doi.org/10.1175/1520-0493(2002)130<2905:TDVAWS>2.0.CO;2).
- Wu, T.-C., H. Liu, S. J. Majumdar, C. S. Velden, and J. L. Anderson, 2014: Influence of assimilating satellite-derived atmospheric motion vector observations on numerical analyses and forecasts of tropical cyclone track and intensity. *Mon. Wea. Rev.*, **142**, 49–71, <https://doi.org/10.1175/MWR-D-13-00023.1>.
- , C. S. Velden, S. J. Majumdar, H. Liu, and J. L. Anderson, 2015: Understanding the influence of assimilating subsets of enhanced atmospheric motion vectors on numerical analyses and forecasts of tropical cyclone track and intensity with an ensemble Kalman filter. *Mon. Wea. Rev.*, **143**, 2506–2531, <https://doi.org/10.1175/MWR-D-14-00220.1>.
- Zhang, D.-L., and H. Chen, 2012: Importance of the upper-level warm core in the rapid intensification of a tropical cyclone. *Geophys. Res. Lett.*, **39**, L02806, <https://doi.org/10.1029/2011GL050578>.
- Zhang, F., Y. Weng, J. F. Gamache, and F. D. Marks, 2011: Performance of convection-permitting hurricane initialization and prediction during 2008–2010 with ensemble data assimilation of inner-core airborne Doppler radar observations. *Geophys. Res. Lett.*, **38**, L15810, <https://doi.org/10.1029/2011GL048469>.
- Zhu, Y., and Coauthors, 2016: All-sky microwave radiance assimilation in NCEP's GSI analysis system. *Mon. Wea. Rev.*, **144**, 4709–4735, <https://doi.org/10.1175/MWR-D-15-0445.1>.